

Direct observation and rational design of nucleation behavior in addressable self-assembly

Martin Sajfutdinow,^{1,2} William M. Jacobs,³ Aleks Reinhardt,⁴ Christoph Schneider,¹ and David M. Smith¹

¹Fraunhofer Institute for Cell Therapy and Immunology IZI,

Department of Diagnostics, Perlickstraße 1, 04103 Leipzig, Germany

²Faculty of Chemistry and Mineralogy, Leipzig University, Johannisallee 29, 04103 Leipzig, Germany

³Department of Chemistry and Chemical Biology, Harvard University,
12 Oxford Street, Cambridge, Massachusetts 02138, United States

⁴Department of Chemistry, University of Cambridge, Lensfield Road, Cambridge, CB2 1EW, United Kingdom

In order to optimize a self-assembly reaction, it is essential to understand the factors that govern its pathway. Here, we examine the influence of nucleation pathways in a model system for addressable, multicomponent self-assembly based on a prototypical ‘DNA-brick’ structure. By combining temperature-dependent dynamic light scattering and atomic force microscopy with coarse-grained simulations, we show how subtle changes in the nucleation pathway profoundly affect the yield of the correctly formed structures. In particular, we can increase the range of conditions over which self-assembly occurs by utilizing stable multi-subunit clusters that lower the nucleation barrier for assembling subunits in the interior of the structure. Consequently, modifying only a small portion of a structure is sufficient to optimize its assembly. Due to the generality of our coarse-grained model and the excellent agreement that we find with our experimental results, the design principles reported here are likely to apply generically to addressable, multicomponent self-assembly.

Increasingly complex structures can now be created by self-assembly [1, 2], from nanostructures with tailored physicochemical properties, such as photonic crystals [3], to quasicrystals [4]. In the limit where every subunit in a target structure is unique and bonds strongly with specific partners, such self-assembled structures are said to be ‘addressable’. Thus far, this degree of specificity has been demonstrated most impressively by experiments on ‘DNA bricks’ [5], in which portions of single-stranded DNA molecules are designed to hybridize uniquely with complementary sequences on strands that occupy neighboring positions in the target structure. Modular nanostructures comprising thousands of distinct strands can be formed in this way, and because the location of each molecule in the target structure is precisely known, these structures can be functionalized at a nanometer length scale.

In addition to providing control over the geometry of the target structure, the use of addressable building blocks makes it possible to exert greater control over the *mechanism* of self-assembly [6]. Because each interaction between subunits can be individually tuned, addressable structures provide a useful platform for exploring the determinants of self-assembly pathways more generally [7]. Considerable progress has been made in this direction using computer simulations [8–16] and statistical mechanics [17, 18] to study coarse-grained models of addressable systems. In particular, coarse-grained modeling has predicted that nucleation barriers¹ are likely to play a particularly important role in addressable self-assembly, since in their absence, the large number of building blocks with similar bonding strengths can instead lead to widespread kinetic trapping and aggregation [9, 17]. These models have further shown that addressable systems often have highly non-classical nucleation barriers and well-defined critical nuclei [13, 17]. However, the microscopic nature of a self-assembly process is challenging to study experimentally. While it is possible to characterize structures by stopping the reaction at a specific point along an annealing ramp [20, 21] for subsequent imaging [22, 23], such approaches cannot be performed *in situ* and may thus perturb the self-assembly process. Furthermore, any assembled struc-

tures must first be isolated before carrying out more detailed analyses, for example by using next-generation sequencing to examine defects in DNA nanostructures [24]. On the other hand, established *in situ* methods can provide information on the kinetics of self-assembly, but only by probing the interactions between pairs of subunits [19, 20, 25–27]. As a result, these interactions must then be extrapolated to describe the assembly of the complete structure.

In this work, we demonstrate that dynamic light scattering (DLS) can be used to track the collective assembly of addressable structures in greater detail. Unlike alternative *in situ* techniques, DLS provides a sensitive means of probing the complete distribution of multi-strand cluster sizes throughout the course of the annealing protocol. Consequently, by applying DLS to DNA-brick self-assembly and validating these results using atomic force microscopy (AFM), we are able to analyze the nucleation process as a function of temperature and assembly time. Combining these results with extensive simulations, we show that it is possible to control the nucleation behavior rationally, with dramatic consequences for the yield of assembled structures. In particular, we demonstrate that the self-assembly mechanism can be optimized by altering the connections among a specific subset of subunits, which modifies the free-energy barrier for structure nucleation. The simplicity of our coarse-grained model suggests that these design principles are transferable to any multicomponent system where the interactions between subunits can be programmed.

RESULTS

Minor changes in nanostructure design strongly affect the yield and quality of self-assembly

As a model system, we examined the self-assembly of a 16-helix DNA cuboid. Following the canonical ‘DNA-brick’ design [5], the fundamental building blocks of this structure are 32-nucleotide (nt) ‘scaffold’ bricks. Each brick comprises four 8-base-pair (bp) domains that hybridize to connect adjacent helices (Fig. 1a). The cross-section was chosen to ensure that bricks on opposite sides of the structure do not interact directly (Fig. 1b), while the high aspect ratio (4 helices \times 4 helices \times 256 bases) facilitates the identification of well-formed structures via atomic force microscopy imaging.

¹ The term ‘nucleation’ in the context of DNA self-assembly is occasionally used to refer to the initial thermodynamically disfavored formation of a few base pairs of a double strand, which is then followed by zipping [19]. We use the term in the more traditional sense to mean the formation of a small portion of the target structure, which leads to structure assembly.

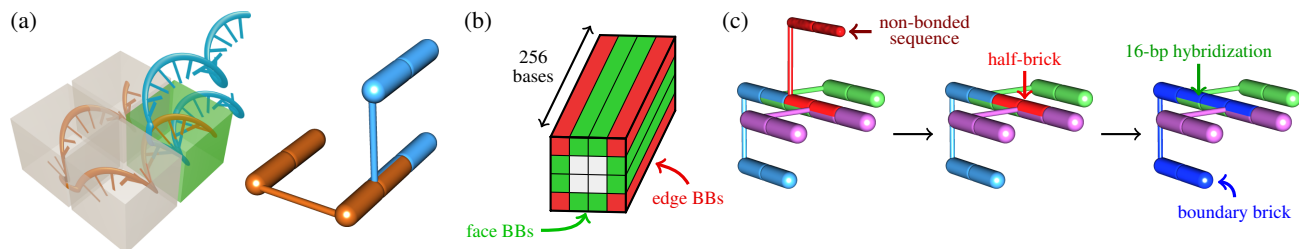


FIG. 1. (a) The bonding pattern between two DNA bricks in a strand and a cylindrical representation. Each molecule is partitioned into four domains (indicated by boxes), while the neighboring bricks are bonded through one pair of domains only (green box). The cylindrical representation shows the same 8-bp hybridization. (b) A schematic illustration of our target structure, highlighting the locations of the ‘edge’ and ‘face’ boundary bricks. (c) A schematic of the boundary brick set-up: the non-interacting DNA sequence at one of the outer surfaces of the target structure is removed and the remainder of that brick is fused with the adjacent brick, resulting in the formation of a 48-nt boundary brick.

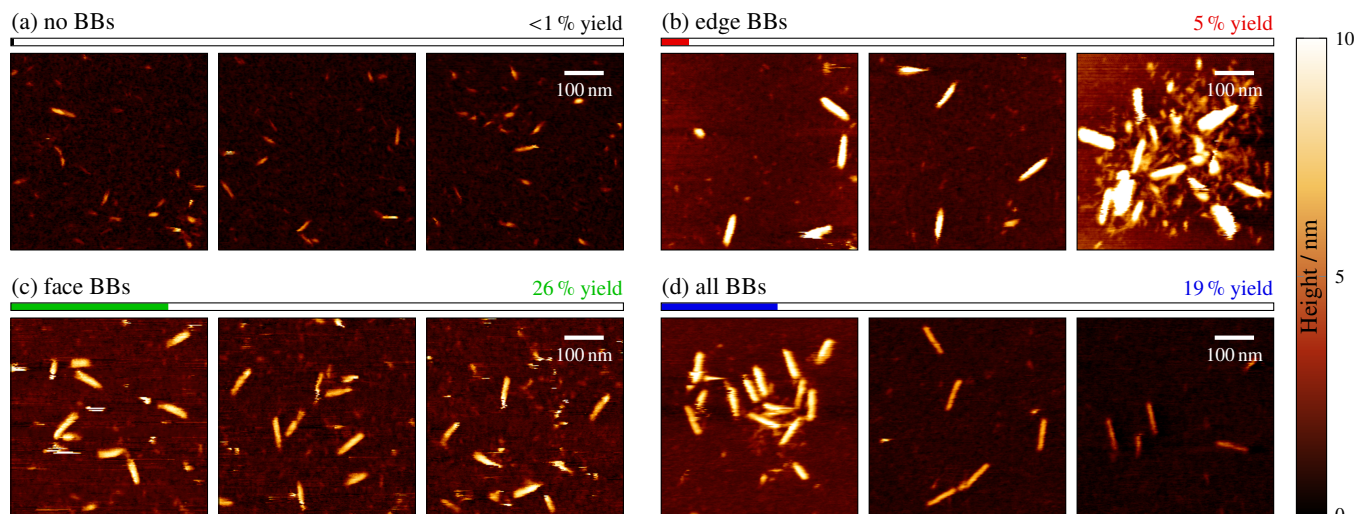


FIG. 2. AFM images taken at the conclusion of a 66 h annealing protocol for each of the four 86 nm-long cuboid designs. No purification was performed on these samples so that incompletely assembled structures can clearly be seen. Typical yields, relative to the total quantity of DNA strands in solution, were estimated via gel electrophoresis and are shown for each system. For the edge-BB system in particular, multi-structure aggregates (shown in the right-most panel) are commonly observed.

To study the factors affecting the self-assembly yield, we designed variants of this cuboid by increasing the lengths of a small number of complementary domains. This was achieved by varying the numbers and types of 48-nt ‘boundary bricks’ (BBs) at the exterior surfaces of the structure (Fig. 1c; see also Fig. S1). In addition to a cuboid composed entirely of scaffold bricks (‘no BBs’), where the 16-bp half-bricks at the exterior of the structure were left unconjugated, we designed variants with boundary bricks forming the corner helices (‘edge BBs’), connecting pairs of helices on the faces of the cuboid (‘face BBs’) or both (‘all BBs’). All variants of the cuboid structure self-assembled to some degree over the course of a 66 h linear annealing ramp (see Sec. SI-1.1). However, AFM imaging (see Sec. SI-1.2) revealed striking differences in the quality of the assembled structures (Fig. 2). The all-BB, face-BB and edge-BB designs resulted in the assembly of many copies of structures with the expected aspect ratio, while designs without boundary bricks yielded a negligible number of such structures (see Sec. SI-1.3 and Fig. S2).

Tracking structure assembly via DLS

To obtain information on the self-assembly process, we used DLS to probe the size of structures as a function of temperature during the annealing ramp. These measurements provide insight into the growth of clusters of hybridized strands without requiring the introduction of intercalating dyes or other additives

that might alter structure assembly. Because sub-micron-sized particles scatter visible light in the Rayleigh limit, where the scattering intensity scales as the sixth power of the particle size, DLS is also highly sensitive to small populations of large clusters. These features of DLS therefore allowed us to detect the initial formation of the target cuboids during the annealing protocol without perturbing the assembly process.

At each temperature step, we obtained the auto-correlation function from a time series of light-scattering intensity measurements in order to extract a distribution of decay rates. Given the low concentration of macromolecules in our experiments ($\sim 0.2\%$ by volume), we assumed that the free diffusion of particles in the suspension was not affected by hydrodynamic interactions, so that the decay rates could be related to the translational diffusion coefficients of independent multi-strand clusters [28]. For ease of interpretation, we present these distributions in terms of the hydrodynamic radius R_h of a spherical particle with an equivalent diffusion coefficient. Since determining the decay rate distribution from the auto-correlation function requires additional assumptions on the smoothness of the cluster-size distribution, we used multiple regularization methods to verify the robustness of our results (Fig. S3; see Sec. SI-1.4).

We first determined the reference cluster-size distribution for a purified sample of assembled all-BB cuboids (Fig. 3a,i). This distribution is peaked at a hydrodynamic radius of 21.5 nm, which matches the expected size of a fully assembled cuboid ($R_h \sim 20$ nm; see Methods). This distribution also agrees with

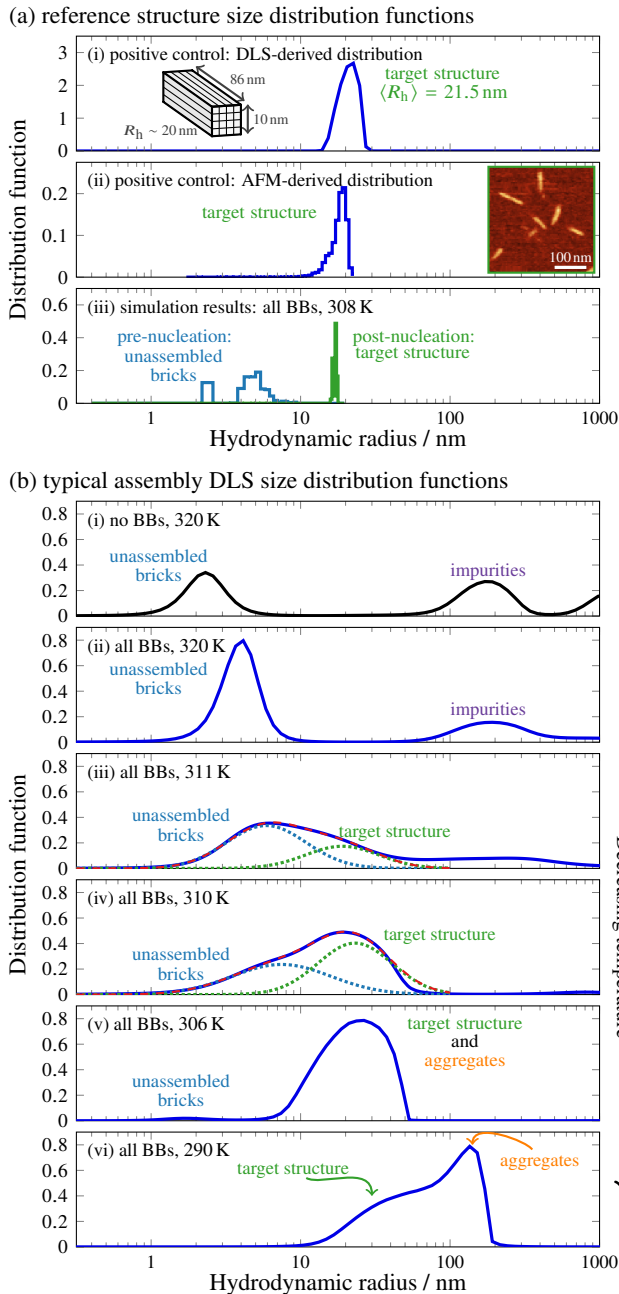


FIG. 3. (a) Reference intensity-weighted size distribution functions for a purified all-BB sample, determined by DLS (panel i) and calculated from AFM images (panel ii) and Monte Carlo simulations (panel iii). Insets show the dimensions of the target structure and a representative AFM image. In panel iii, the blue curves indicate the metastable cluster-size distribution prior to nucleation, while the green curves show the equilibrated distribution after the target structure has assembled. The gap between the monomer and dimers in the pre-nucleation distribution is an artifact of the lattice simulations. (b) Representative intensity-weighted distribution functions at decreasing temperatures. At high temperatures (panels i and ii), the no-BB distribution indicates unhybridized scaffold strands, while the all-BB distribution is dominated by small clusters of BBs, as seen in the pre-nucleation Monte Carlo simulations. At intermediate temperatures (panels iii and iv), the distribution can be fitted to a sum of two Gaussians (red dashes), which correspond to the unassembled (blue dots) and target-structure (green dots) populations, respectively. At lower temperatures (panels v and vi), a small population of larger aggregates skews the intensity-weighted distribution, but the contribution from the target structure can still be seen in panel vi.

the ideal distribution calculated from AFM images of purified all-BB cuboids (Fig. 3a,ii), in which all imaged particles were

treated as rigid cylinders (see Methods). The broadening of the reference distribution relative to this ideal distribution is likely due to the effects of particle anisotropy on light scattering, which we have not attempted to account for here.

We next used lattice Monte Carlo simulations of an established coarse-grained model [9] to calculate ideal cluster-distribution functions of the all-BB system, equilibrated both before and after nucleation of the target structure (Fig. 3a,iii; see Methods). Consistent with prior simulations [9, 17], we found that intermediate cluster sizes, with R_h between 8 and 15 nm, are unstable. Consequently, the size distribution is either peaked near 5 nm, corresponding to small clusters of primarily boundary bricks, or 18 nm, corresponding to a mostly complete target structure. Because these simulations consider a single copy of the target structure, the system can only be in one state at a time; however, in a larger system with many copies of each brick, the assembly of a fraction of all structures would result in a bimodal cluster-size distribution. The simulation results therefore suggest that the R_h distribution can be used to resolve the target structure during an assembly experiment. We note that the discretization of small cluster sizes in the unassembled population is an artifact of the lattice model and is not expected to be seen in experiments.

Typical size-distribution functions determined by DLS similarly show that R_h is a suitable order parameter for identifying complete structures (Fig. 3b). At high temperatures (Fig. 3b,i-ii), before nucleation occurs, we observed a single peak (ignoring high-molecular-weight impurities) corresponding to individual strands and small clusters. In particular, in the no-BB system, the peak matches the expected size of a flexible 32-nt strand, $R_h \sim 2.7$ nm. Then, upon decreasing the temperature, a new population suddenly appeared at $R_h \sim 20$ nm. As expected from our simulation results, the cluster-size distributions at these intermediate temperatures are well described by bimodal fits to a linear combination of Gaussian functions (Fig. 3b,iii-iv). In particular, the means of the Gaussian fits coincide with the reference unassembled and target-structure distributions; however, the fitted populations are considerably broader than the reference distributions. This is likely a consequence of the conservative regularization method used in the analysis of the autocorrelation data, which tends to smooth the resulting distributions, as well as heterogeneity due to incomplete assembly. To confirm our interpretation of the bimodal cluster-size distributions, we discuss a complementary validation strategy based on an analysis of AFM images below and in the Supplementary Material.

At lower temperatures (Fig. 3b,v-vi), particles with effective hydrodynamic radii larger than ~ 40 nm begin to contribute to the distribution. This shift toward larger R_h is likely due to the formation of aggregates of fully or partially assembled structures. However, we emphasize that because of the sixth-power dependence of the light scattering intensity on the particle size, only a small fraction of aggregated structures is needed to skew the cluster-size distribution substantially. For the same reason, the large- R_h impurities present at higher temperatures (Fig. 3b,i,ii) are extremely rare. Nevertheless, despite the tendency of the structure and aggregate peaks to merge due to our conservative choice of regularization method, the population of target structures can still be identified from the shoulder of the cluster-size distribution at 290 K (Fig. 3b,vi).

Evidence for nucleation and growth

For each structure variant, we determined both the cluster-size distribution via DLS and the extent of subunit hybridization via fluorescence measurements (see Sec. SI-2) as a function of

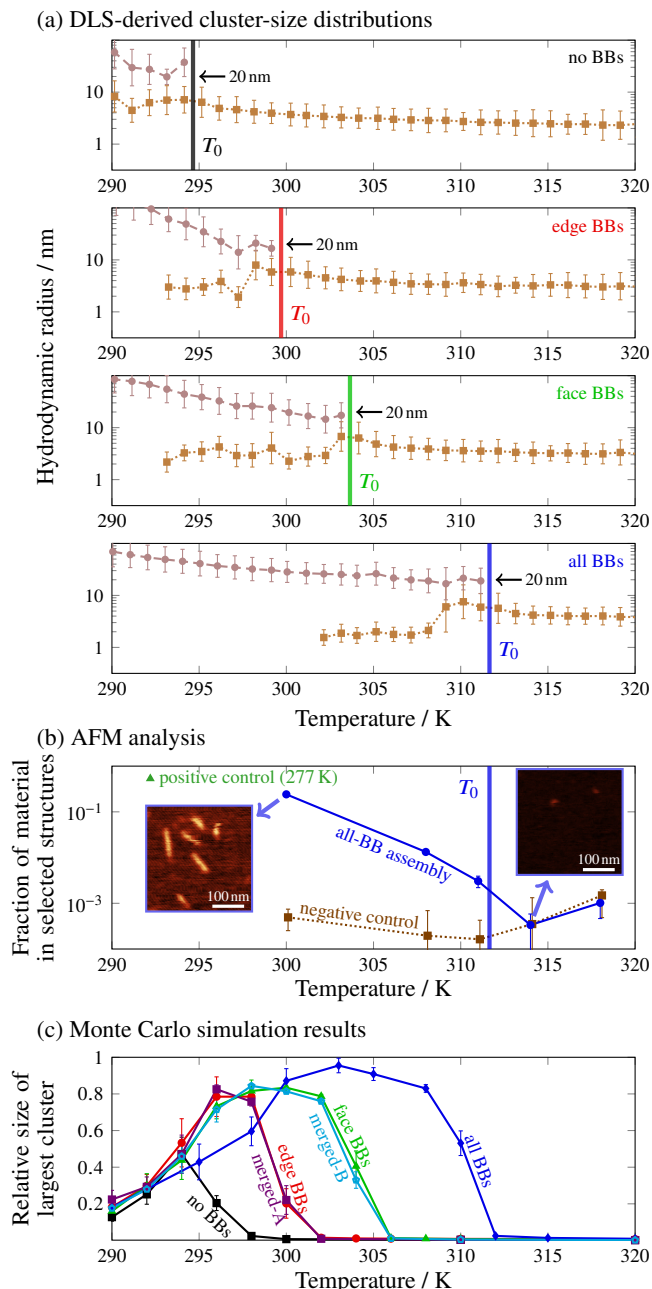


FIG. 4. (a) Unimodal and bimodal cluster-size distributions determined via DLS following a 15.2 h annealing protocol. Points and error bars show the mean hydrodynamic radii and standard deviations, respectively, of the Gaussian fits to the unassembled and target structure populations (cf. Fig. 3b,iii-iv) at each temperature. For each system, T_0 indicates the temperature at which the higher- R_h population first appears during the annealing protocol. (b) The volume fraction comprising target cuboids, relative to the total volume of material, determined from AFM analysis of the all-BB system. All samples were rapidly quenched for imaging from the indicated temperatures. The target-structure volume fraction of the positive-control all-BB sample (green triangle) and non-hybridizing oligonucleotides (negative control, dotted line) were calculated in the same way, and the error bars show the estimated standard error based on Poisson statistics. Insets show representative portions of the raw AFM images. (c) The size of the largest correctly bonded cluster from Monte Carlo simulations. Each data point corresponds to the average of ten independent simulations in the long time limit, once nucleation has occurred, with error bars showing the standard deviation. The ‘merged’ curves refer to fixed edge dimers, as discussed in the text and Fig. S1.

temperature over the course of a 15.2 h linear annealing protocol. We observed prominent peaks in the fluorescence response of systems containing BBs at high temperatures (> 330 K). This

behavior could be attributed to the formation of stable high-temperature dimers, in which the elongated boundary bricks (Fig. 1c) stably hybridize to other bricks in continuous 16- or 24-bp domains (Fig. S4). However, in DLS experiments, we did not observe any substantial change in the overall scattering intensity at temperatures above 315 K (Fig. S5), implying that the assembly of complete structures does not take place at these temperatures. Nevertheless, DLS did resolve differences in the unassembled populations. At temperatures where only a single peak was present (excluding contributions from any impurities in the system), we found that the mean hydrodynamic radius $\langle R_h \rangle$ of the no-BB system increased from ~ 2.5 nm to ~ 4 nm upon cooling, reflecting an increasing fraction of scaffold-strand dimers (Fig. 4a). Similarly, the single-peak $\langle R_h \rangle$ in systems with boundary bricks increased from $\gtrsim 3$ nm to ~ 5 nm upon cooling, consistent with the presence of larger pre-formed BB dimers.

In each system, we observed the sudden appearance of a second peak in the cluster-size distribution at a temperature T_0 (Fig. 4a). This feature appeared at the same temperature in multiple annealing runs for each system, with the exception of the no-BB structure, where T_0 varied by ~ 2 K across three runs. As in the example distributions shown in Fig. 3b,iii-iv, the mean hydrodynamic radius of this population, determined by fitting a linear combination of Gaussian functions, coincided with the expected size of the target structure in all systems. Because of the comparable scattering intensities of the two populations at T_0 , we ascribed this second peak to the scattering of a relatively small number of essentially complete target structures. The target-structure $\langle R_h \rangle$ remained nearly constant for at least 3 K below T_0 in all systems before increasing above 20 nm, most likely due to aggregation as discussed above. By contrast, the fluorescence response (Fig. S4) did not provide definitive insights into the assembly of the complete structure for any cuboid variant.

Importantly, our experiments indicate that the target structures do not grow gradually as a function of temperature. Instead, DLS reveals that the transition from having all unassembled subunits to having some complete structures occurs discontinuously. The unassembled population remains easily detectable over a temperature range of approximately 10 K below T_0 for each structure, indicating that not all subunits are incorporated into complete structures at T_0 . For the no-BB, edge-BB, and face-BB systems, the mean R_h of this population is comparable to the mean R_h of unassembled strands above T_0 . By contrast, the mean R_h of this population decreased in the all-BB system near 308 K, suggesting that only scaffold strands remained unassociated with target structures or aggregates below this temperature.

To validate further our interpretation of the cluster-size distributions obtained from DLS, we performed a complementary analysis based on AFM imaging of the all-BB system at selected temperatures. Using AFM images of quenched and immobilized samples, we estimated the fraction of the total volume of imaged particles comprising target structures. We first determined appropriate criteria, using the areas and aspect ratios of imaged particles, for identifying correctly assembled cuboids in images of a purified sample (Fig. S6). We then applied these criteria to estimate the target-structure volume fraction as a function of the temperature from which the sample was quenched (Fig. 4b; see also Fig. S7). Because the rapid quenching involved in the preparation of the samples likely affects the particle-size distribution and AFM does not reliably distinguish single-stranded DNA from the background, this method cannot be used to assess the volume fraction of assembled structures quantitatively. In addition, image analysis inevitably identifies some false target structures. However, by comparing the calculated volume fractions with a negative control of approximately 200 non-

hybridizing, similar-length oligonucleotides, which accounts for sample-preparation and imaging artifacts, we verified that the target structures are indeed present at temperatures below, but not above, T_0 . The low estimated volume fraction (approximately 0.3 %) just below T_0 is also consistent with the roughly equal areas of the intensity-weighted unassembled and target-structure populations seen in DLS (Fig. 3b,iii-iv), demonstrating the sensitivity of DLS to small populations of large clusters. This analysis therefore corroborates our primary conclusions from the DLS experiments and supports our interpretation of the $R_h \approx 20$ nm population. The remainder of our study is based on DLS data, since this technique can be performed *in situ* without perturbing the assembly process.

Comparison with coarse-grained Monte Carlo simulations

To observe the self-assembly process in greater detail, we simulated the assembly of a coarse-grained DNA-brick model using Monte Carlo dynamics at constant temperature [9]. Previous studies [9, 17] of this model have found that self-assembly proceeds via nucleation and growth, whereby clusters that are intermediate between unassembled strands and nearly complete target structures are thermodynamically unstable. In particular, the nucleation step, which requires the formation of a critical multi-strand cluster, is a thermally activated rare event and thus determines the highest temperature at which self-assembly can occur. Therefore, following an approach established for simulating structures with BBs [14], we studied the nucleation of cuboid designs analogous to those used in our DLS experiments, using a single copy of the target structure and hybridization parameters chosen to mimic the experimental conditions (see Methods).

Remarkably, we found that for each cuboid variant, the highest temperature at which nucleation occurs in our simulations is in nearly quantitative agreement with the temperature at which the $R_h \approx 20$ nm population first appears in the DLS experiments. This can be seen by comparing the temperature at which the average cluster size sharply increases in Fig. 4c with the corresponding T_0 in Fig. 4a. It is important to note that, unlike in the experiments, all simulations were initialized from an unassembled solution with the total experimental monomer concentration at each temperature. The simulated trajectories should thus only be compared to the initial formation of target structures near T_0 during the annealing ramp, after which monomer depletion must be taken into account. In simulations initiated at lower temperatures, kinetic trapping arising from subunit misbonding tends to inhibit structure nucleation, as evidenced by the decreased average cluster sizes at temperatures below ~ 295 K (Fig. 4c). In contrast with the variations in nucleation behavior, the effects of misbonding are essentially independent of the structure design in our simulations.

Pre-formed clusters modify nucleation barriers

Based on the evidence of high-temperature hybridization (see Sec. SI-2), we hypothesized that the presence of pre-formed clusters involving BBs might play a key role in determining nucleation behavior. Similar behavior is exhibited in our simulations, where BB dimers form nearly completely prior to structure nucleation (Fig. S8). We further tested this idea by running simulations in which BB dimers were merged into permanently bonded units, mimicking the result of high-temperature hybridization in the experimental system. To this end, simulations with merged edge BBs ('merged-A'; see Fig. S1) confirmed that

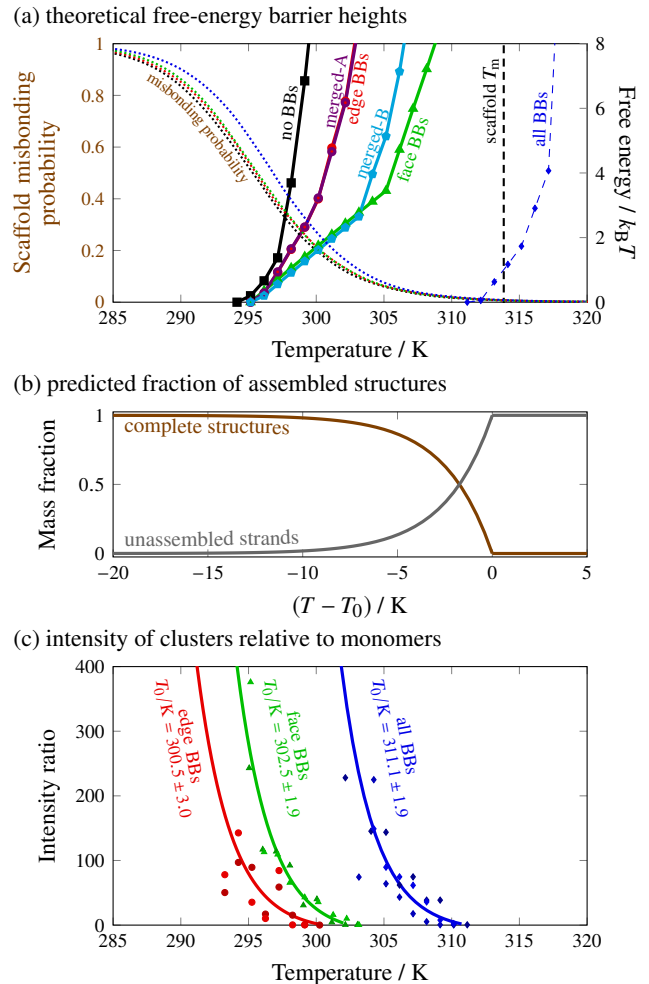


FIG. 5. (a) The height of the nucleation barrier, at the initial free-strand concentration, as a function of temperature from theoretical calculations. The all-BB barrier refers to the nucleation of a network of boundary bricks, as discussed in the text. We also show the predicted scaffold melting temperature, T_m , and the median probability that a scaffold strand forms at least one mis-interaction in the absence of successful nucleation. (b) The predicted evolution of the unassembled-strand and complete-structure populations over the course of a nucleation-limited annealing protocol, determined from the nucleation-barrier calculations (see Sec. SI-3). (c) The ratio of the experimentally determined intensities of the two populations as a function of temperature, alongside an exponential fit $c(\exp[-a(T - T_0)] - 1)$ for each system, with $1/a = 2.5$ K (see Sec. SI-3); points are shown for multiple annealing runs.

nucleation in this system is analogous to the edge-BB structure (Fig. 4c).

This hypothesis is supported by free-energy calculations using a discrete combinatorial model [17, 18], in which each distinct subunit type is represented as a node in an abstract graph that describes the connectivity of the target structure. Assuming that all 16- and 24-bp domains hybridize completely at high temperatures, we merged the corresponding pairs of subunits to account for changes in the local subunit connectivity due to the incorporation of each type of boundary brick. We then used this model to calculate the free-energy barrier to nucleation by further assuming that the number of subunits in a partially assembled cluster is a good reaction co-ordinate (see Methods). These free-energy calculations predict that the heights of the nucleation barriers, and thus the logarithms of the nucleation rates, vary rapidly with temperature (Fig. 5a). Furthermore, the relative ordering of the nucleation-barrier curves for the no-BB, edge-BB, and face-BB systems is consistent with the

DLS and simulation results, indicating that merging subunits via high-temperature hybridization is sufficient to modify the nucleation behavior. For comparison, we show the predicted melting temperature T_m below which the scaffold-strand core of the cuboid is thermodynamically stable; the model predicts that successful nucleation always requires that the system be supersaturated by lowering the temperature below the scaffold-strand T_m . We also show that the effects of strand misbonding are captured by a simple estimate of the probability of pairwise mis-interactions (see Methods). As in our simulations, the misbonding probabilities are nearly independent of boundary-brick incorporation.

Interestingly, we found that the assembly of the all-BB structure follows a three-step mechanism that is not well described by a one-dimensional free-energy landscape. In this system, pairs of pre-formed multimers can hybridize with one another via multiple 8-bp domains. Consequently, bonding networks that are dominated by BBs begin to form at temperatures where all single 8-bp hybridizations are unstable, leading to extensive boundary-brick bonding and large cluster-size fluctuations in simulations above 310 K (Fig. S8). Our simulations show that the nucleation of the interior of the structure then occurs in a separate assembly step, at temperatures slightly below the predicted scaffold-strand melting temperature, T_m . Because the theoretical results assume a one-dimensional order parameter, we only show the predicted free-energy barrier that pertains to the formation of an initial network of boundary bricks in the all-BB system in Fig. 5a.

Nucleation strongly affects self-assembly yield

Because our free-energy calculations predict that the height of the nucleation barrier also depends strongly on the subunit concentration, the nucleation rate is expected to decrease with monomer depletion [6]. The changing concentration of unassembled subunits is therefore predicted to result in the continued production of complete structures at temperatures below T_0 in an annealing ramp where nucleation is rate-limiting (Fig. 5b; see Sec. SI-3). This prediction takes into account the temperature scaling derived from the calculated nucleation barriers and the temperature dependence of the hybridization free energies (Fig. S9), assuming perfect stoichiometry and zero aggregation. To test this prediction, we integrated the experimentally determined total scattering intensity associated with each peak in the cluster-size distribution and, assuming that this intensity is proportional to the number density, determined the ratio of large- to small- R_h populations. The trends shown in Fig. 5c for the edge-BB, face-BB and all-BB structures follow the predictions of our free-energy calculations, as the intensity ratios are consistent with the functional form and temperature scaling shown in Fig. 5b. Since there must be some leftover subunits due to imperfect stoichiometry (measured to be approximately $\pm 10\%$), we did not expect the unassembled population to decay to zero in the experimental system. However, the associated intensity did not attain a constant level before the small- R_h peak fell below the detection range of the instrumentation.

These observed variations in nucleation behavior therefore provide a likely explanation for the extreme differences in yields among our structural variants and the similarity between the ranking of the final yields and the order of the initial assembly transitions. At any given temperature, only a fraction of the potential structures ultimately form because nucleation slows as large clusters are produced; consequently, decreasing the temperature by means of an annealing protocol is necessary to continue driving nucleation of additional structures. However,

our simulations and no-BB DLS measurements indicate that misbonding dominates below 295 K. Structure designs that nucleate at higher temperatures thus benefit from a broader temperature range over which nucleation can occur.

Nucleation behavior and kinetic stability can be independently tuned

The differences among our cuboid variants do not affect the thermodynamic properties of the scaffold strands, which comprise the bulk of the structure. However, incorporating boundary bricks can, in principle, increase the kinetic stability of assembled structures. To examine this effect, we reversed the temperature ramp and used DLS to track the melting of assembled structures. We observed the complete melting of all structures in solution, as evidenced by the disappearance of the $R_h \sim 20$ nm population, at considerably higher temperatures than the assembly transitions (Fig. 6a). The complete melting transitions, T_m , of the cuboid variants occurred in the reverse order of the assembly transitions, T_0 , indicating that a strong bonding network of boundary bricks provides a kinetic barrier to disassembly. However, the differences in melting temperatures were generally smaller for structures that nucleate at lower temperatures, suggesting that the boundary bricks affect disassembly to a lesser extent than they affect nucleation.

Melting simulations of fully formed structures show similar trends (Fig. 6b). Analysis of the simulation trajectories reveals that scaffold bricks at the edges of the no-BB and face-BB structures disassemble first. The face-BB structures therefore lose bricks at lower temperatures than the edge-BB structures, although the face boundary bricks provide a larger barrier to complete disassembly. Disassembly occurs most abruptly in the case of the all-BB structures, with bricks initially dissociating from the unprotected ends of the structure. Consistent with the assembly simulations, the all-BB structures disassemble via a three-step disassembly mechanism, in which large networks of boundary-brick dimers persist for a few degrees above the apparent melting temperature (Fig. 6b).

To distinguish between the effects of nucleation and kinetic stability, we designed the ‘half-face-BB’ cuboid shown schematically in Fig. 6c. By incorporating face BBs on only one half of the structure, we predicted that we would see improved nucleation behavior, as with the full face-BB structure, but reduced kinetic stability. DLS confirmed that this structure initially nucleates at a temperature close to the face-BB T_0 (Fig. 6c), in agreement with our simulations and free-energy calculations (Fig. S10). The assembly yield (Fig. S11) is dramatically improved relative to the no-BB structure, but is less than that of the face-BB structure, presumably because one half of the cuboid is not protected by boundary bricks and is thus more susceptible to aggregation from low-temperature misbonding.

Importantly, DLS reveals that the half-face-BB structure melts *before* the edge-BB structure does, implying that the lack of boundary-brick protection on one face facilitates disassembly of the complete structure. Comparing the half-face-BB and no-BB systems, which have similar melting temperatures, highlights the crucial role of enhanced nucleation, as opposed to increased stability, in improving the yield. More generally, this example demonstrates that the nucleation behavior and thermal stability of DNA-brick nanostructures can be independently tuned.

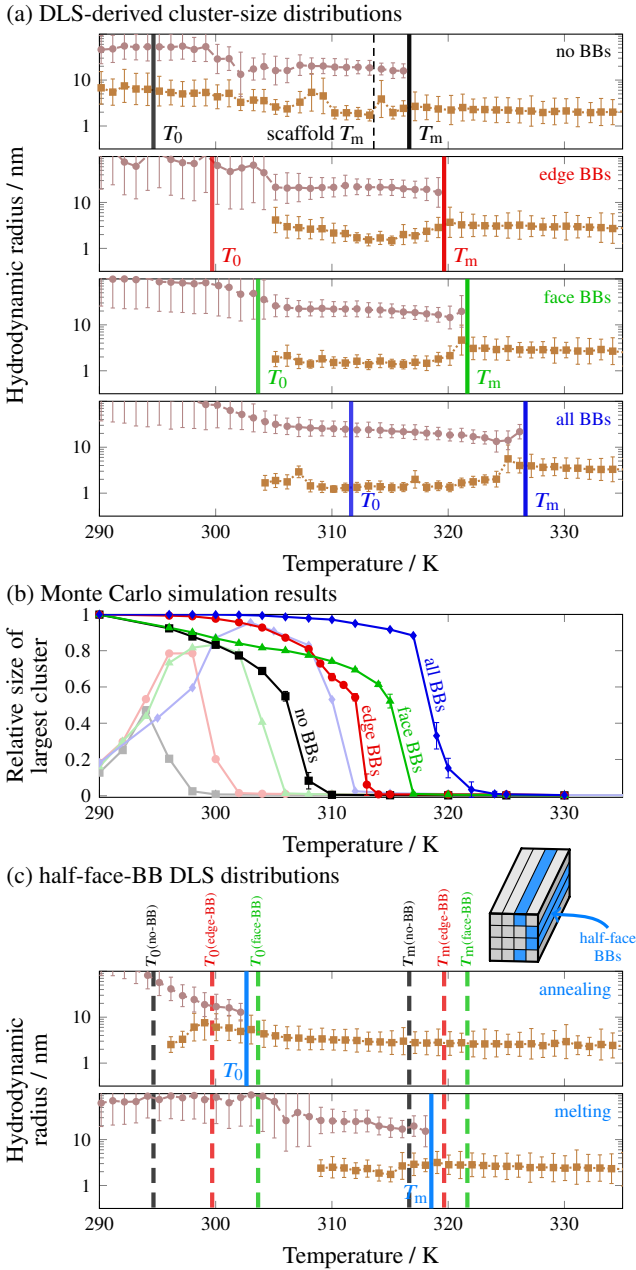


FIG. 6. (a) Cluster-size distributions determined from DLS melting experiments (cf. Fig. 4a). The temperatures at which all structures have melted, T_m , are compared to the initial assembly temperatures, T_0 . The no-BB structures melt completely at a temperature close to the predicted scaffold-strand T_m (dashed line). (b) The hysteresis in the size of the structure as a function of temperature can be seen by comparing the long-time-limit average cluster sizes in simulations initialized from pre-assembled structures (solid lines) and from an unassembled solution (faded lines from Fig. 4c). In (c), we show the annealing (top) and melting (bottom) cluster-size distributions for a half-face BB system. The inset shows a schematic illustration of the BB locations. The temperatures T_0 and T_m for the no-BB, edge-BB, and face-BB systems are shown by dashed vertical lines for comparison. Importantly, the order in which the half-face-BB and edge-BB structures nucleate is different from the order in which they melt.

Nucleation pathways are determined by the connectivity of pre-formed clusters

To identify the microscopic origin of the differences in nucleation behavior, we calculated minimum-free-energy pathways using our theoretical model (Fig. 7). For each structure, we determined the free-energy as a function of the number of independent subunits and the number of pre-formed dimers at a temperature

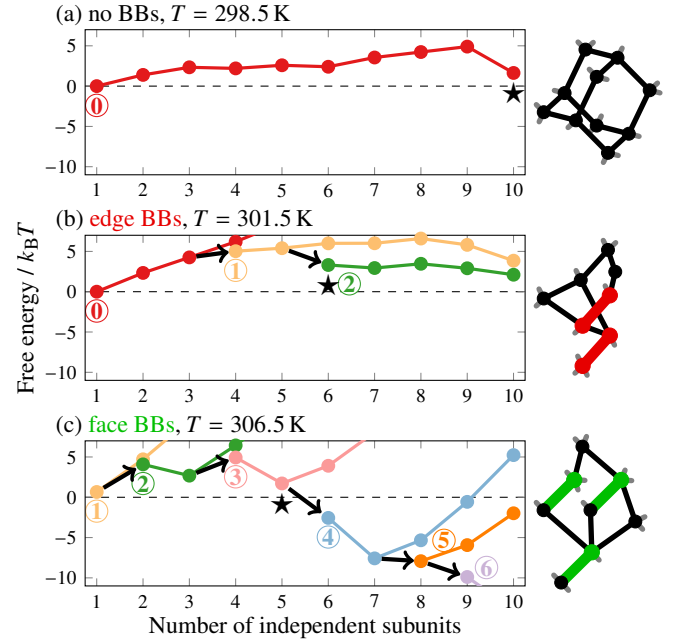


FIG. 7. The free energy as a function of cluster size and composition from theoretical calculations, showing that the minimum-free-energy self-assembly pathway depends on the presence of pre-formed multimers. The number of pre-formed multimers within each cluster is indicated by the ringed numbers and the corresponding colors. Clusters on the minimum-free-energy pathway grow by incorporating one independent subunit at a time, which may be either a single scaffold brick (following a colored line) or a pre-formed multimer (following an arrow). For ease of comparison, each free-energy landscape is shown at a temperature at which the nucleation barrier is approximately $5 k_B T$. The post-critical nuclei, which coincide with the first subunit addition after the highest point on the minimum-free-energy path, are indicated by stars. Schematic diagrams of representative post-critical nuclei, with pre-formed multimers indicated by colored lines, are shown on the right. For a comparison with simulation trajectories, see Fig. S12; representative pathways are also illustrated in Figs S13–S15.

where the nucleation barrier is approximately $5 k_B T$, which is comparable to the barrier height at which nucleation was observed in previous simulations of this model [9, 17]. The typical order in which dimers and scaffold strands are incorporated into a growing cluster is indicated by the minimum-free-energy nucleation pathways in Fig. 7 and illustrated in Figs S13–S15. Importantly, these calculations allow us to identify typical post-critical nuclei, the smallest multi-strand clusters that are more likely to grow via strand addition than to dissociate and whose formation is thus the rate-limiting step on each predicted nucleation pathway. The topologies of these clusters are shown in Fig. 7; however, because there are many topologically equivalent clusters within each structure, with unique sequences for the hybridized segments, there are numerous post-critical nuclei comprising distinct strands with slightly different free energies.

These landscapes reveal crucial differences between the edge-BB and face-BB structures, which contain the same number of 48-nt BBs, and point to the key role of the connections between the pre-formed dimers and interior scaffold strands. Topologically, this difference arises from the fact that face-BB dimers contain segments that directly connect to the fully-interior scaffold strands, whereas the edge-BB dimers are only indirectly connected to these ‘core’ strands (see Fig. S1). Because each subunit addition results in a loss of translational entropy, the free energy on a nucleation pathway only decreases when multiple 8-bp bonds are formed with a single subunit addition, resulting in a topologically closed cycle. In the absence of boundary bricks,

our previous work has shown that the post-critical nucleus at typical nucleation temperatures is a tricyclic cluster comprising twelve 8-bp bonds and ten subunits [17]. Yet by incorporating pre-formed dimers, fewer independent subunits are needed to reach a post-critical nucleus. The 8-bp bonds can thus be weaker, leading to an elevated nucleation temperature. Despite the fact that the edge-BB and face-BB dimers have the same number of 8-nt domains for binding to other subunits, the topologies of the minimum-free-energy clusters in these structures are different: the edge-BB structures require six subunits, including two BB dimers, to form a post-critical bicyclic cluster (Fig. 7b), while face-BB structures only require five subunits, including three dimers (Fig. 7c). Consistent with the predicted pathways, simulation trajectories show that BB dimers comprise a larger fraction of the post-critical clusters in the face-BB structure than in the edge-BB structure (Fig. S12). We can also exclude the concentration of pre-formed dimers as the determining factor by comparing the half-face-BB and edge-BB structures, as these systems contain the same number of pre-formed dimers but nucleate at significantly different temperatures.

Based on these findings, we hypothesized that by changing the local connectivity of the edge BBs, we might be able to reproduce the enhanced nucleation behavior of the face-BB structure. To test this hypothesis directly, we ran simulations of the edge-BB system in which we explicitly merged each edge dimer with one of its neighboring scaffold strands in the target structure (Fig. S1). The only difference between this structure ('merged-B'; see Fig. S1) and a normal edge-BB dimer is that this additional connection to the interior scaffold strands, which would otherwise need to form spontaneously during the nucleation process and thus entail a loss of translational entropy, has been fixed in place. This modification leads to post-critical nuclei that comprise five independent subunits, resulting in assembly behavior that is nearly analogous to that of the face-BB structure (Figs 4c and 5a). Thus, although this particular modification would be difficult to achieve experimentally using DNA bricks, our simulations and theory show that the addition of a single connection to the interior of the structure can alter the nucleation behavior significantly.

Design rules for enhanced nucleation

Based on our experimental, simulation and theoretical findings, we propose four design rules for enhancing the nucleation behavior and assembly yield in addressable systems:

1. The key determinant of the structure yield is the separation between the initial nucleation and misbonding temperatures. While the misbonding temperature is set by the pairwise interactions and the subunit concentrations, the nucleation temperature can be tuned through rational structure design. By contrast, changes to the subunit interactions that uniformly affect both correct and incorrect bonds are unlikely to improve the yield.
2. Altering the 'valency' of specific subunits to create multi-step pathways, for example by forming boundary-brick dimers at high temperatures, is a viable strategy for controlling nucleation, because it can change the number of independent subunits in the critical nucleus. On the other hand, tuning individual bond strengths is a less effective strategy for selecting a specific nucleation pathway, since the number of parallel pathways grows superextensively with the size of the target structure.
3. Controlling the topology of the critical nuclei is crucial. It may not be optimal simply to add high-valency subunits, as in

the case of the edge BBs. Instead, efficient nucleation requires that the critical nuclei contain many stabilizing bonds but few subunits, favoring the formation of free-energy-reducing topological cycles earlier in the nucleation pathway. This is achieved in the case of the face-BB and merged-B structures by maximizing the number of bonds between the pre-formed dimers and the interior scaffold bricks.

4. Only a small portion of a structure needs to be optimized to achieve enhanced nucleation behavior. For example, comparison of the half-face-BB and no-BB systems shows that modifying fewer than 20 % of the subunits drastically raises the initial nucleation temperature and markedly improves the yield.

DISCUSSION

By combining dynamic light scattering with a coarse-grained theoretical model, we have shown that the ultimate yield of correctly assembled structures is largely determined by the nucleation pathway. As a specific example, we have investigated the role of nucleation kinetics in addressable self-assembly by modifying the bonding characteristics of specific subunits at the boundaries of a DNA-brick nanostructure. We have shown that the location and design of the altered subunits determine the free-energy landscape for self-assembly and control the temperature at which nucleation first becomes feasible. Moreover, the nearly quantitative agreement between the predictions of a coarse-grained model and our experimental results allows us to rationalize these striking effects on the self-assembly behavior.

Taken together, our experiments and modeling establish practical design principles for improving the self-assembly of addressable nanostructures. In a typical annealing protocol, structures have a limited time and temperature window in which to form: at high temperatures, a large free-energy barrier inhibits nucleation, while at low temperatures, self-assembly is limited by kinetic arrest. The key to successful self-assembly is to increase the width of the temperature window over which nucleation can occur, thereby maximizing the thermodynamic segregation between the critical nucleation step and detrimental misbonding. This can be achieved by stabilizing the critical nuclei, which allows self-assembly to proceed when the subunit interactions are still relatively weak. To demonstrate this principle with DNA bricks, we have shown that the increased valency of boundary-brick dimers, which assemble at temperatures much higher than those at which nucleation can occur, lowers the free-energy barrier to nucleation by decreasing the entropic cost of forming a critical number of stabilizing bonds. However, this strategy only works if the high-valency subunits are optimally connected to the remainder of the structure, as evidenced by the difference in nucleation behavior between the edge-BB and face-BB structures. More generally, our results show that it is possible to use a relatively small number of high-valency subunits to design the nucleation pathway rationally and suggest that this approach is not necessarily limited to manipulating bricks at the boundaries of a structure.

Our experiments provide the first explicit characterization of three-dimensional structure nucleation in the context of addressable self-assembly. This advance has been enabled by our use of DLS, which allows us to probe multi-strand structure growth, as opposed to the fraction of inter-subunit bonds that are formed at a given temperature. This distinction is particularly evident in the system evaluated here, where the initial nucleation temperature does not necessarily correlate with the maximal increase in DNA base-pairing. Furthermore, the cluster-size distributions that we obtain from DLS resolve the populations of

unincorporated bricks, complete structures and aggregates, making it possible to track the evolution of these species throughout the course of an annealing protocol. Together with the complementary AFM-based validation, these measurements provide experimental evidence that DNA bricks self-assemble via a nucleation-and-growth mechanism and reveal the relationship between the design of addressable structures and their nucleation kinetics.

The excellent agreement between the predictions of our theoretical model and our experimental results demonstrates that our coarse-grained approach captures the fundamental physics of addressable self-assembly. This agreement gives us confidence that our theory and simulations can be used to guide rational design strategies for complex self-assembly, not only in the context of DNA bricks specifically, but — precisely because of the generality of the models used — also for optimizing addressable systems more broadly. We anticipate that the principles established here will therefore guide efforts to design the nucleation behavior of colloidal systems such as supramolecular and nanoparticle lattices [29–31], protein nanostructures [32] and DNA-origami-based systems with programmable interactions [33]. For example, analogous pre-nucleation clusters could be constructed by forming high-temperature bonds between caged nanoparticles [34] or by directly introducing a small population of dumbbell-like subunits. Alternatively, the connectivity of specific subunits could be altered by changing the arrangement of directional patches on colloidal particles [35]. As we have demonstrated here, successful implementation will require knowledge of the effects of such modifications on the critical nucleus for structure assembly, which dictates the optimal design strategy for any specific system.

MATERIALS AND METHODS

In the Supplementary Material, we describe how we chose the DNA sequences for the strands for each system studied. We also provide complete details of the annealing protocols, the conditions used in AFM and gel electrophoresis, and the protocols used when obtaining fluorescence and light scattering data in the Extended Methods. Supporting data are available at the University of Cambridge Data Repository [36].

Structure annealing

Structures were assembled using a strand concentration of 153 nM per sequence in a buffer of 15 mM MgCl₂, 0.5 mM EDTA and 5 mM Tris at pH 8. Strands in the reaction mixture were denatured at 90 °C for 10 min and then gradually cooled via either (i) a 15.2 h protocol (reciprocal cooling rate 12 min K⁻¹) or (ii) a 66 h protocol (reciprocal cooling rate 52 min K⁻¹).

Atomic force microscopy

Samples from annealing protocol (ii) were immobilized for 10 min on poly-L-ornithine coated mica discs and imaged in liquid in intermittent contact mode using a BioLever Mini cantilever and JPK Nanowizard 3 AFM.

Agarose gel electrophoresis

Structures were analyzed via gel electrophoresis on a gel made from 2 wt% agarose in 0.5 × TBE and 10 mM MgCl₂.

Electrophoresis was performed at 80 V and 4 °C for 2 h. The gel was post-stained with ethidium bromide and the yield was estimated using GelBandFitter software [37].

Fluorescence annealing

Annealing protocol (i) was used for fluorescence annealing experiments with 10 nM SYBR green I solution [38] added to the reaction mixture. The fluorescence signal was measured as a function of temperature with an ABI Prism 7900HT-Fast Real Time PCR system at 488 nm.

Static and dynamic light scattering

Using annealing protocol (i), light scattering measurements were performed in the last 2 min of each temperature step. Light scattering of 20 μL samples was measured using a Malvern Zetasizer NanoZSP apparatus at an angle of 173°. For DLS, the intensity auto-correlation function was computed from 12 measurements at 10 s intervals. Cluster-size distributions were determined from the auto-correlation data using multiple regularization methods [39] to verify their robustness (Fig. S3).

Reference hydrodynamic radius calculations

The hydrodynamic radius of a freely jointed chain is $R_h = (3\pi N\ell^2/128)^{1/2}$ [40], where N is the number of segments and ℓ is the length of a segment. To estimate the hydrodynamic radius for single-stranded DNA, we used a typical Kuhn length of $\ell = 4.45$ nm and length per DNA base of $b = 0.676$ nm [41]. A 32-nt scaffold brick comprises $N \approx 32 \times b/\ell = 4.9$ Kuhn segments and hence $R_h \approx 2.7$ nm; for a 48-nt boundary brick, $R_h \approx 3.3$ nm. Since the quantities ℓ and b used here do not correspond to the temperatures and salt concentrations used in our experiments, these calculations only provide us with rough estimates of the magnitudes of R_h for unhybridized strands.

For cylindrical structures, the translational diffusion coefficient is [42]

$$D_{\text{tr}} = \frac{k_B T [\ln(L/d) + \gamma(d/L)]}{3\pi\eta L}, \quad (1)$$

where k_B is the Boltzmann constant, T is the absolute temperature, η is the viscosity of the medium, L is the cylinder length, d is the cylinder diameter, and γ is an end-effect correction given by $\gamma(x) = 0.312 + 0.565x + 0.1x^2$. Assuming that the hydrodynamics of a cylinder are well approximated by a sphere with hydrodynamic radius R_h , we can equate this diffusion coefficient to that of a sphere using the Stokes–Einstein–Smoluchowski equation,

$$D_{\text{tr}} = \frac{k_B T}{6\pi\eta R_h}, \quad (2)$$

leading to an approximate hydrodynamic radius of

$$R_h = (L/2) [\ln(L/d) + \gamma(d/L)]^{-1}. \quad (3)$$

Assuming a typical interhelical spacing of ~ 2.5 nm [43], our target structure can be treated as a cylinder with circumscribed diameter $d \approx 15$ nm and length $L \approx 86$ nm, resulting in an expected hydrodynamic radius of $R_h \approx 20$ nm.

Image analysis

Particle identification in AFM images was done by applying the threshold function of Gwyddion version 2.5.0 [44]. The reference R_h distribution shown in Fig. 3a,ii was calculated using the lengths, L , and aspect ratios, $L/d \approx L^2/A$, where A is the projected area, of the particles assuming the cylindrical formula given above; particles with a minimum width greater than 25 nm, which correspond to overlapping structures, were excluded from this calculation. To compute the distribution function, particles were weighted by R_h^6 , and the distribution was normalized.

To calculate the fraction of correctly assembled structures in an AFM image, we selected all particles that satisfied constraints on both the projected area, $450 \text{ nm}^2 \leq A \leq 1500 \text{ nm}^2$, and the circularity, $0.145 \leq 4A/\pi L^2 \leq 0.375$. These limits were chosen based on the distribution of imaged particles in the purified all-BB system (Fig. S6). All particles were weighted by their volumes, as determined by the Laplacian background basis feature of Gwyddion, in order to assess the total fraction of the material contained in the selected particles. To reduce background noise, we also required that the area of the selected particles measured at half the particle height be at least $0.3A$ and the average height be at least 2 nm. Standard errors were assigned to the yields by assuming a Poisson distribution based on the calculated yield and the absolute number of selected particles.

Monte Carlo simulations

We performed lattice Metropolis Monte Carlo simulations of DNA brick self-assembly using a coarse-grained potential and dynamics that preserve the cluster-size dependence of the diffusion rates [9, 12, 14]. Every DNA brick was represented as a ‘patchy particle’ with four patches corresponding to its four domains, each of which was assigned a specific unique sequence, chosen randomly but with the constraint that patches that are bonded in the target structure have complementary DNA sequences. The interaction energies correspond to the hybridization free energies of these sequences obtained from the SantaLucia parameterization [45]. When computing these hybridization free energies, we used a salt correction [46] corresponding to salt concentrations of $[\text{Na}^+] = 0$ and $[\text{Mg}^{2+}] = 0.015 \text{ M}$. In the simulations reported here, we used a system of 550 bricks in a box with lattice parameter $150a$, where $a\sqrt{3}$ is the shortest possible distance between any two particles. Assuming typical brick dimensions of $(a\sqrt{3})^3 \approx 2.5 \text{ nm} \times 2.5 \text{ nm} \times 2.7 \text{ nm}$ [5, 13], this set-up corresponds to a concentration of 153 nM. We accounted for boundary bricks by imposing rigid bonds between dimers (or, in certain cases, larger multimers) of these patchy particles that would be merged into a single boundary brick in experiment [14]. Particles connected in this way remain at a fixed distance and dihedral angle to one another throughout the simulation. Non-interacting patches on the outside of the target structure were assigned poly-T sequences. We estimated a Kirkwood-like [47] hydrodynamic radius of each cluster by computing

$$R_h \approx \frac{N(N-1)}{2} \left[\sum_{\langle ij \rangle} \frac{1}{r_{ij}} \right]^{-1} + 0.5 \times 2.7 \text{ nm}, \quad (4)$$

where N is the number of particles in the cluster, $\langle ij \rangle$ indicates a summation over every pair of particles i and j in the cluster, and r_{ij} is the distance between them on the lattice, using the typical brick dimensions given above to determine that $a \approx 1.48 \text{ nm}$

for the lattice unit of length. The monomer R_h is set to 2.7 nm, while the addition of $0.5 \times 2.7 \text{ nm}$ in (4) crudely accounts for the dangling ends of monomers at one of the bases of the structure, which are not otherwise accounted for in the coarse-grained model. (4) thus predicts that a scaffold brick dimer will have a hydrodynamic radius of $R_h \approx 3.9 \text{ nm}$.

Free-energy calculations

All free-energy calculations were carried out using the abstract-graph model described in Ref. 17. The free energy of a particular cluster g , comprising a set of subunits $\mathcal{V}(g)$, is

$$\frac{F_g}{k_B T} = - \sum_{\substack{i,j \in \mathcal{V}(g) \\ j \in \mathcal{E}(i)}} \frac{\varepsilon_{ij}}{2} - (N_g - 1) \ln \frac{\rho}{q_{\text{rot}}} + (N_g - B_g - 1) \ln q_{\text{dih}}, \quad (5)$$

where N_g is the number of subunits in the cluster, $\mathcal{E}(i)$ indicates the set of strands that are neighbors of strand i in the target structure, and the dimensionless bond strengths are $\varepsilon_{ij} = \ln[\exp(-\Delta G_{ij}/k_B T) - 1]$. We determined ΔG_{ij} for each pair of complementary sequences i, j in the experimental systems using the SantaLucia parameterization described above. Each subunit, with concentration ρ , was assumed to have $q_{\text{rot}} = 4$ rotational degrees of freedom, and each single bond was assumed to have $q_{\text{dih}} = 3$ dihedral degrees of freedom; these values were chosen to match the Monte Carlo simulations. B_g refers to the number of ‘bridges’ in the graph g [17]. The cluster free energy as a function of the number of correctly bonded subunits is

$$F(N) = -k_B T \ln \sum_g \mathbf{1}(N_g = N) \exp(-F_g/k_B T), \quad (6)$$

where $\mathbf{1}(\cdot)$ is the indicator function. $F(N)$ was calculated using the efficient Monte Carlo approach described in Ref. 17. Similarly, in Fig. 7a, the cluster free energy was calculated as a function of the total number of subunits and the number of pre-formed dimers.

The melting temperature T_m of an infinite lattice of scaffold strands with co-ordination number $z = 4$ was estimated based on the mean of the 8-bp scaffold-strand hybridization free energies by solving the equation

$$(z/2) \overline{\Delta G(T_m)} = k_B T_m \ln(\rho/q_{\text{rot}} q_{\text{dih}}). \quad (7)$$

Misbonding calculations

We used a two-state model (i.e. bonded or not bonded) to calculate the probability that a strand forms at least one misinteraction, assuming that no domains are correctly hybridized. We found the longest complementary subsequence for each pair of strands i and j that are not neighbors in the target structure and calculated the associated hybridization free energy, $\Delta G_{\text{min},ij}$. [In cases where there are multiple complementary subsequences $\{s\}$ of the same length for a given pair of strands, we calculated the Boltzmann-weighted sum, $\Delta G_{\text{min},ij} = -k_B T \ln \sum_s \exp(-\Delta G_s/k_B T)$.] We then computed the probability that a strand i forms a misinteraction, $p_{\text{mis},i}$,

$$p_{\text{mis},i} = Z_{\text{mis},i} / (1 + Z_{\text{mis},i}), \quad (8)$$

$$Z_{\text{mis},i} = \sum_{j \notin \mathcal{E}(i)} \rho \exp(-\Delta G_{\text{min},ij}/k_B T). \quad (9)$$

When computing the probability of scaffold-strand misbonding, the index i represents a scaffold strand, while the index j runs over all strands in the system. This approximate approach captures the competition between designed and incorrect bonding seen in the simulations (Fig. 4c) remarkably well.

ACKNOWLEDGMENTS

We thank Daan Frenkel for helpful discussions. This work was supported by the Engineering and Physical Sciences Re-

search Council [Programme Grant EP/I001352/1], the European Regional Development Fund [100185665], Fraunhofer Attract Funding [601683] and the National Institutes of Health [Grant F32GM116231].

-
- [1] S. Whitelam and R. L. Jack, ‘The statistical mechanics of dynamic pathways to self-assembly,’ *Annu. Rev. Phys. Chem.* **66**, 143 (2015).
- [2] D. Frenkel, ‘Order through entropy,’ *Nat. Mater.* **14**, 9 (2015).
- [3] J. Zhang, Z. Sun, and B. Yang, ‘Self-assembly of photonic crystals from polymer colloids,’ *Curr. Opin. Colloid In.* **14**, 103 (2009); E. Sowade, T. Blaudeck, and R. R. Baumann, ‘Self-assembly of spherical colloidal photonic crystals inside inkjet-printed droplets,’ *Cryst. Growth Des.* **16**, 1017 (2016).
- [4] J. I. Urgel, D. Écija, G. Lyu, R. Zhang, C.-A. Palma, W. Auwärter, N. Lin, and J. V. Barth, ‘Quasicrystallinity expressed in two-dimensional coordination networks,’ *Nat. Chem.* **8**, 657 (2016); A. Reinhardt, J. S. Schreck, F. Romano, and J. P. K. Doye, ‘Self-assembly of two-dimensional binary quasicrystals: A possible route to a DNA quasicrystal,’ *J. Phys.: Condens. Matter* **29**, 014006 (2017); P. F. Damasceno, S. C. Glotzer, and M. Engel, ‘Non-close-packed three-dimensional quasicrystals,’ *J. Phys.: Condens. Matter* **29**, 234005 (2017).
- [5] Y. Ke, L. L. Ong, W. M. Shih, and P. Yin, ‘Three-dimensional structures self-assembled from DNA bricks,’ *Science* **338**, 1177 (2012); L. L. Ong, N. Hanikel, O. K. Yaghi, C. Grun, M. T. Strauss, P. Bron, J. Lai-Kee-Him, F. Schueder, B. Wang, P. Wang, J. Y. Kishi, C. Myhrvold, A. Zhu, R. Jungmann, G. Bellot, Y. Ke, and P. Yin, ‘Programmable self-assembly of three-dimensional nanostructures from 10,000 unique components,’ *Nature* **552**, 72 (2017).
- [6] W. M. Jacobs and D. Frenkel, ‘Self-assembly of structures with addressable complexity,’ *J. Am. Chem. Soc.* **138**, 2457 (2016).
- [7] L. Cademartiri and K. J. M. Bishop, ‘Programmable self-assembly,’ *Nat. Mater.* **14**, 2 (2015).
- [8] R. Schulman and E. Winfree, ‘Programmable control of nucleation for algorithmic self-assembly,’ *SIAM J. Comput.* **39**, 1581 (2010); J. Zenk and R. Schulman, ‘An assembly funnel makes biomolecular complex assembly efficient,’ *PLoS ONE* **9**, e111233 (2014).
- [9] A. Reinhardt and D. Frenkel, ‘Numerical evidence for nucleated self-assembly of DNA brick structures,’ *Phys. Rev. Lett.* **112**, 238103 (2014).
- [10] Z. Zeravcic, V. N. Manoharan, and M. P. Brenner, ‘Size limits of self-assembled colloidal structures made using specific interactions,’ *Proc. Natl. Acad. Sci. U. S. A.* **111**, 15918 (2014).
- [11] J. Madge and M. A. Miller, ‘Design strategies for self-assembly of discrete targets,’ *J. Chem. Phys.* **143**, 044905 (2015); ‘Optimising minimal building blocks for addressable self-assembly,’ *Soft Matter* **13**, 7780 (2017).
- [12] A. Reinhardt, C. P. Ho, and D. Frenkel, ‘Effects of co-ordination number on the nucleation behaviour in many-component self-assembly,’ *Faraday Discuss.* **186**, 215 (2016).
- [13] A. Reinhardt and D. Frenkel, ‘DNA brick self-assembly with an off-lattice potential,’ *Soft Matter* **12**, 6253 (2016).
- [14] H. K. Wayment-Steele, D. Frenkel, and A. Reinhardt, ‘Investigating the role of boundary bricks in DNA brick self-assembly,’ *Soft Matter* **13**, 1670 (2017).
- [15] D. J. Wales, ‘Atomic clusters with addressable complexity,’ *J. Chem. Phys.* **146**, 054306 (2017).
- [16] P. Fonseca, F. Romano, J. S. Schreck, T. E. Ouldridge, J. P. K. Doye, and A. A. Louis, ‘Multi-scale coarse-graining for the study of assembly pathways in DNA-brick self assembly,’ *J. Chem. Phys.* **148**, 134910 (2018).
- [17] W. M. Jacobs, A. Reinhardt, and D. Frenkel, ‘Communication: Theoretical prediction of free-energy landscapes for complex self-assembly,’ *J. Chem. Phys.* **142**, 021101 (2015); ‘Rational design of self-assembly pathways for complex multicomponent structures,’ *Proc. Natl. Acad. Sci. U. S. A.* **112**, 6313 (2015).
- [18] W. M. Jacobs and D. Frenkel, ‘Self-assembly protocol design for periodic multicomponent structures,’ *Soft Matter* **11**, 8930 (2015).
- [19] A. V. Pinheiro, J. Nangreave, S. Jiang, H. Yan, and Y. Liu, ‘Steric crowding and the kinetics of DNA hybridization within a DNA nanostructure system,’ *ACS Nano* **6**, 5521 (2012).
- [20] J.-P. J. Sobczak, T. G. Martin, T. Gerling, and H. Dietz, ‘Rapid folding of DNA into nanoscale shapes at constant temperature,’ *Science* **338**, 1458 (2012).
- [21] J. M. Majikes, J. A. Nash, and T. H. LaBean, ‘Search for effective chemical quenching to arrest molecular assembly and directly monitor DNA nanostructure formation,’ *Nanoscale* **9**, 1637 (2017).
- [22] J. Song, J.-M. Arbona, Z. Zhang, L. Liu, E. Xie, J. Elezgaray, J.-P. Aime, K. V. Gothelf, F. Besenbacher, and M. Dong, ‘Direct visualization of transient thermal response of a DNA origami,’ *J. Am. Chem. Soc.* **134**, 9844 (2012).
- [23] T. Kato, R. P. Goodman, C. M. Erben, A. J. Turberfield, and K. Namba, ‘High-resolution structural analysis of a DNA nanostructure by cryoEM,’ *Nano Lett.* **9**, 2747 (2009).
- [24] C. Myhrvold, M. Baym, N. Hanikel, L. L. Ong, J. S. Gootenberg, and P. Yin, ‘Barcode extension for analysis and reconstruction of structures,’ *Nat. Commun.* **8**, 14698 (2017).
- [25] X. Wei, J. Nangreave, S. Jiang, H. Yan, and Y. Liu, ‘Mapping the thermal behavior of DNA origami nanostructures,’ *J. Am. Chem. Soc.* **135**, 6165 (2013).
- [26] S. Jiang, F. Hong, H. Hu, H. Yan, and Y. Liu, ‘Understanding the elementary steps in DNA tile-based self-assembly,’ *ACS Nano* **11**, 9370 (2017).
- [27] X. Wei, J. Nangreave, and Y. Liu, ‘Uncovering the self-assembly of DNA nanostructures by thermodynamics and kinetics,’ *Acc. Chem. Res.* **47**, 1861 (2014).
- [28] B. J. Berne and R. Pecora, *Dynamic light scattering: with applications to chemistry, biology, and physics* (Wiley, London, 1976).
- [29] R. J. Macfarlane, B. Lee, M. R. Jones, N. Harris, G. C. Schatz, and C. A. Mirkin, ‘Nanoparticle superlattice engineering with DNA,’ *Science* **334**, 204 (2011).
- [30] M. Huang, C.-H. Hsu, J. Wang, S. Mei, X. Dong, Y. Li, M. Li, H. Liu, W. Zhang, T. Aida, W.-B. Zhang, K. Yue, and S. Z. D. Cheng, ‘Selective assemblies of giant tetrahedra via precisely controlled positional interactions,’ *Science* **348**, 424 (2015).
- [31] H. Lin, S. Lee, L. Sun, M. Spellings, M. Engel, S. C. Glotzer, and C. A. Mirkin, ‘Clathrate colloidal crystals,’ *Science* **355**, 931 (2017).
- [32] J. B. Bale, S. Gonen, Y. Liu, W. Sheffler, D. Ellis, C. Thomas, D. Cascio, T. O. Yeates, T. Gonen, N. P. King, and D. Baker, ‘Accurate design of megadalton-scale two-component icosahedral protein complexes,’ *Science* **353**, 389 (2016).
- [33] T. Gerling, K. F. Wagenbauer, A. M. Neuner, and H. Dietz, ‘Dynamic DNA devices and assemblies formed by shape-complementary, non-base pairing 3D components,’ *Science* **347**, 1446 (2015).
- [34] W. Liu, M. Tagawa, H. L. Xin, T. Wang, H. Emamy, H. Li, K. G. Yager, F. W. Starr, A. V. Tkachenko, and O. Gang, ‘Diamond family of nanoparticle superlattices,’ *Science* **351**, 582 (2016).
- [35] Y. Wang, Y. Wang, D. R. Breed, V. N. Manoharan, L. Feng, A. D. Hollingsworth, M. Weck, and D. J. Pine, ‘Colloids with valence and specific directional bonding,’ *Nature* **491**, 51 (2012).
- [36] M. Sajfutdinow, W. M. Jacobs, A. Reinhardt, C. Schneider, and D. M. Smith, ‘Research data supporting “Direct observation and rational design of nucleation behavior in addressable self-assembly” [Dataset],’ doi:10.17863/cam.22991.
- [37] M. I. Mitov, M. L. Greaser, and K. S. Campbell, ‘GelBandFitter – A computer program for analysis of closely spaced electrophoretic

- and immunoblotted bands,' *Electrophoresis* **30**, 848 (2009).
- [38] H. Zipper, H. Brunner, J. Bernhagen, and F. Vitzthum, 'Investigations on DNA intercalation and surface binding by SYBR Green I, its structure determination and methodological implications,' *Nucleic Acids Res.* **32**, e103 (2004).
- [39] S. Hansen, 'DLSanalysis.org: a web interface for analysis of dynamic light scattering data,' *Eur. Biophys. J.* **47**, 179 (2018).
- [40] I. Teraoka, *Polymer solutions: an introduction to physical properties* (Wiley, New York, 2002).
- [41] Q. Chi, G. Wang, and J. Jiang, 'The persistence length and length per base of single-stranded DNA obtained from fluorescence correlation spectroscopy measurements using mean field theory,' *Physica A* **392**, 1072 (2013).
- [42] J. García de la Torre and V. A. Bloomfield, 'Hydrodynamic properties of complex, rigid, biological macromolecules: Theory and applications,' *Q. Rev. Biophys.* **14**, 81 (1981).
- [43] S. Fischer, C. Hartl, K. Frank, J. O. Rädler, T. Liedl, and B. Nickel, 'Shape and interhelical spacing of DNA origami nanostructures studied by small-angle X-ray scattering,' *Nano Lett.* **16**, 4282 (2016).
- [44] D. Nečas and P. Klapetek, 'Gwyddion: an open-source software for SPM data analysis,' *Cent. Eur. J. Phys.* **10**, 181 (2012).
- [45] J. SantaLucia Jr and D. Hicks, 'The thermodynamics of DNA structural motifs,' *Annu. Rev. Biophys. Biomol. Struct.* **33**, 415 (2004).
- [46] R. T. Koehler and N. Peyret, 'Thermodynamic properties of DNA sequences: Characteristic values for the human genome,' *Bioinformatics* **21**, 3333 (2005).
- [47] J. G. Kirkwood, 'The general theory of irreversible processes in solutions of macromolecules,' *J. Polym. Sci.* **12**, 1 (1954).
- [48] M. Sajfutdinow, K. Uhlig, A. Prager, C. Schneider, B. Abel, and D. M. Smith, 'Nanoscale patterning of self-assembled monolayer (SAM)-functionalised substrates with single molecule contact printing,' *Nanoscale* **9**, 15098 (2017).
- [49] S. W. Provencher, 'A constrained regularization method for inverting data represented by linear algebraic or integral equations,' *Comput. Phys. Commun.* **27**, 213 (1982).
- [50] W. Wang, T. Lin, S. Zhang, T. Bai, Y. Mi, and B. Wei, 'Self-assembly of fully addressable DNA nanostructures from double crossover tiles,' *Nucleic Acids Res.* **44**, 7989 (2016).
- [51] Y. Ke, L. L. Ong, W. Sun, J. Song, M. Dong, W. M. Shih, and P. Yin, 'DNA brick crystals with prescribed depths,' *Nat. Chem.* **6**, 994 (2014).
- [52] S. Giglio, P. T. Monis, and C. P. Saint, 'Demonstration of preferential binding of SYBR Green I to specific DNA fragments in real-time multiplex PCR,' *Nucleic Acids Res.* **31**, e136 (2003).
- [53] D. Suh and J. B. Chaires, 'Criteria for the mode of binding of DNA binding agents,' *Bioorg. Med. Chem.* **3**, 723 (1995).
- [54] K. M. Ririe, R. P. Rasmussen, and C. T. Wittwer, 'Product differentiation by analysis of DNA melting curves during the polymerase chain reaction,' *Anal. Biochem.* **245**, 154 (1997).

SUPPLEMENTARY INFORMATION

1 EXTENDED METHODS

If not otherwise noted, chemicals were purchased from Sigma Aldrich Chemie GmbH (Munich, Germany).

1.1 Annealing protocols

DNA sequences for the target cuboid structure are given in Sec. SI-5. For the all-BB system, sequences were taken from Ref. 5 (Table S8), and DNA strands were appropriately decoupled to split the relevant boundary bricks for the face-BB, edge-BB and no-BB systems. All sequences were purchased from Eurofins Genomics in 100 μM stocks in ddH₂O, and then pooled using a Tecan Genesis Workstation 150 liquid handling robot. We used a strand concentration of 153 nM in 1 \times assembly buffer, i.e., a solution of 15 mM MgCl₂, 0.5 mM EDTA and 5 mM Tris, pH 8. The strand solution was denatured at 90 °C for 10 min and then gradually cooled. We used two linear cooling protocols: (i) in the 15.2 h protocol, the reciprocal cooling rate was 12 min K⁻¹, and (ii) in the 66 h protocol, it was 52 min K⁻¹. The annealed samples were stored at 4 °C.

Prior to the reference DLS measurement (positive control), the all-BB sample assembled in the 66 h protocol was supplemented with 2.5 mM EDTA to reduce high-molecular-weight contamination. In the context of DLS experiments, we therefore refer to this sample as ‘purified’.

Prior to the reference AFM imaging (positive control), the all-BB sample assembled in the 66 h protocol was ultrafiltered using Amicon (UFC510024, Millipore, Merck KGaA, Darmstadt, Germany) filter units, with a molecular weight cut-off of 100 kDa, to reduce the fraction of small particle contamination and to improve the image quality. To this end, the assembled sample was mixed with pre-chilled 1 \times assembly buffer to the maximum admitted volume and centrifuged for 10 min at 14 000g at 4 °C. Subsequently, the flowthrough was discarded, and the filter unit was loaded with buffer and centrifuged again. This process was repeated three times in total. Finally, the concentrated filtrate was eluted at 1000g for 2 min at 4 °C.

1.2 Atomic force microscopy

Samples were prepared following the 66 h annealing protocol. A freshly cleaved mica disc was coated with 100 μL of 0.5 wt% poly-L-ornithine solution for 5 min and rinsed three times with 1 \times assembly buffer. In order to be able to image samples in liquid mode, an acrylic glass ring was glued by Thin Pour (Reprorubber) onto a slide to surround the mica disc and form a fluid cell. For each sample, 1.5 pmol per brick was deposited on the coated mica for 10 min. Afterwards, the cell was filled with 1 \times assembly buffer and imaged using the JPK Nanowizard 3 atomic force microscope and a BioLever Mini cantilever in intermittent contact mode in liquid. Images were recorded with a target amplitude of 15 nm.

Quenching experiments, designed to stop the hybridization reaction at a given temperature during the annealing protocol, were done by immobilizing 5 μL of the reaction mixture on poly-L-ornithine coated and pre-equilibrated mica discs. As a negative control, the same procedure was performed using a random selection of ssDNA strands that did not contain complementary sequences [48]. For both the all-BB structure and the negative control, samples were quenched from 318 K,

314 K, 311 K, 308 K and 300 K during annealing protocol (i) and imaged by AFM, as described above, at ambient temperature.

1.3 Agarose gel electrophoresis

Assembly of DNA brick structures was confirmed by non-denaturing agarose gel electrophoresis. Samples (300 fmol per brick) were analyzed on a gel made from 2 wt% agarose in 0.5 \times TBE and 10 mM MgCl₂. Electrophoresis was performed at 80 V and 4 °C for 2 h. The gel was post-stained with 0.5 $\mu\text{g mL}^{-1}$ ethidium bromide solution and scanned in using the Intas GDS gel set instrument for structure visualization. To estimate structure yield, the band intensity was approximated by fitting densitometry profiles with an SQP algorithm to Gaussian functions using the GelBandFitter software [37]. The mass of the structure fractions was estimated via a 1 kb standard (GeneRuler, ThermoFischer Scientific) and related to the total mass loaded of 850 ng.

1.4 Static and dynamic light scattering

The same conditions as in the 15.2 h annealing protocol were used and the measurement was performed in the last 2 min of the 12 min cooling step. 20 μL samples were filled into ZEN2112 quartz cuvettes (Malvern), covered by molecular biology grade mineral oil, and sealed with a plastic lid that was further fixed with tape. Light scattering was measured using a Malvern Zetasizer NanoZSP apparatus at an angle of 173°. The viscosity of the samples was determined at five temperatures spanning the region of interest and fitted to $\eta/(10^{-5} \text{ Pa s}) = 1.78 \times \exp[617/(T/\text{K} - 138.5)]$. The refractive index was measured to be 1.331.

For dynamic light scattering, the intensity auto-correlation function was computed from 12 measurements at 10 s intervals. We interpreted the DLS data in the dilute limit by assuming that all particles diffused independently of one another, since the total strand concentration (approximately 40 μM) implies that single strands ($R_h \sim 2.7$ nm) in solution occupied a volume fraction of approximately 0.2 %. We further assumed that, after the initial equilibration period of 10 min, the distribution of cluster sizes remained nearly constant over the DLS measurement period at the end of each temperature step; this assumption is consistent with our observations of rate-limiting structure nucleation.

When analyzing DLS data for solutions comprising a range of particle sizes, the inverse Laplace transform used to obtain a particle size distribution from the intensity auto-correlation function is not uniquely determined [49], and the choice of fitting functions and parameters can affect the final result [39]. We have therefore computed multiple fits to the distribution of hydrodynamic radii using several regularization methods, including a range of different smoothing exponents and a maximum entropy constraint (Fig. S3). We also performed the analysis using the CONTIN algorithm [49] and via entropy maximization with a uniform prior distribution (not shown). Although the agreement is not perfect for the individual data points, the trends for the distributions and the fits to a linear combination of Gaussian functions are nearly the same regardless of the regularization procedure used, indicating that the conclusions drawn from the DLS data are robust with respect to the choice of regularization method. We chose to use the smoothness constraint regularization method recommended in

Ref. 39 with a smoothing exponent of $m = 8/5$ (corresponding to Fig. S3b) for all data reported in the main text.

1.5 Fluorescence annealing

In the fluorescence annealing experiments, the same conditions as in the 15.2 h annealing protocol were used, except that 10 nM SYBR green I solution [38] was added to the strand mixture. SYBR green I in buffer solution was analyzed as a negative control. Samples were placed on a MicroAmp Fast Plate 96-well tray and sealed with adhesive film. The plate was loaded onto the ABI Prism 7900HT-Fast Real Time PCR system, with dye excitation effected by an argon ion laser at 488 nm. The fluorescence signal was detected at 525 nm every 8.5 s and averaged over time at each temperature, and its derivative with respect to temperature was computed numerically. The data were smoothed via a Gaussian filter with a standard deviation of 1.5 K.

2 MONITORING STRAND HYBRIDIZATION

2.1 Fluorescence measurements

We monitored the progress of domain hybridization during the annealing protocol via fluorescence, using SYBR green I as a double-stranded DNA probe (see Sec. SI-1.5) [20]. We observed a dominant maximum in the fluorescence derivative between 335 K and 350 K for all structures with boundary bricks (Fig. S4a), indicating a significant amount of base-pairing at relatively high temperatures. However, as we discuss in the main text, no complete structures were assembled at these temperatures.

Comparison with theoretical annealing curves suggests that the assembly of boundary-brick structures is a two-step process. To demonstrate this, we show in Fig. S4b the temperature derivative of the equilibrium number of base pairs in a solution of monomers and dimers [45, 46], assuming that stable misbonding between non-complementary domains cannot occur (see below). The high-temperature transitions correspond to the hybridization between pairs of boundary bricks (where continuous 24-bp segments are hybridized) or between one scaffold strand and one boundary brick (with 16-bp hybridized segments). Consequently, the assembly of the full structure must occur in the presence of these pre-formed clusters. These calculations also indicate that the fluorescence-signal contributions from each domain length overlap significantly, since the domain melting temperatures vary widely according to their specific sequences, and each hybridization reaction tends to occur over a broad ($\gtrsim 10$ K) range of temperatures. In particular, the theoretical annealing curves predict a broad maximum associated with the 8-bp domains near 295 K.

Analysis of fluorescence data has previously been used to distinguish between single- and multi-step assembly mechanisms for DNA tile systems with varying domain lengths. For example, a similar step-wise assembly process was seen in DX-tile structures comprising short (10- and 11-bp) and long (21-bp) hybridizations, and the presence of two distinct maxima in the fluorescence derivative was interpreted as evidence of hierarchical assembly [50]. By contrast, fluorescence measurements of DNA-brick crystallization using equal-length domains exhibited no evidence of hierarchical self-assembly [51]. In our measurements, there appear to be multiple local maxima in the annealing curves at temperatures below the scaffold-strand $T_m \approx 315$ K, the highest temperature at which our theoretical calculations

predict that a lattice of scaffold strands can be thermodynamically stable. However, these signals are significantly weaker than the higher-temperature hybridizations which dominate the fluorescence signal. Interpreting the lower-temperature maxima is additionally hindered by several known sources of bias, including high background signals [38] and the preferential binding of SYBR green I to GC-rich sequences [52]. Furthermore, the intercalating SYBR green I probes distort the double-helical structure of DNA molecules [53], which increases their melting temperatures [54] and precludes a quantitative analysis.

2.2 Hybridization calculations

All hybridization calculations were carried out using the SantaLucia parameterization and the solution conditions described in the Methods section of the main text. In this section, we consider a two-state model (i.e. bonded or not bonded) for each domain and examine the simple case where pairs of strands hybridize to form dimers, but not larger multimers. We denote the hybridization free energy between complementary domains on a pair of strands i and j by ΔG_{ij} . The equilibrium probability that a strand i is correctly hybridized with its putative neighbor strand j is

$$p_{ij}(T) = \frac{\rho \exp(-\Delta G'_{ij}/k_B T)}{1 + \rho \exp(-\Delta G'_{ij}/k_B T)}, \quad (10)$$

where ρ is the dimensionless strand number density, k_B is the Boltzmann constant, T is the absolute temperature, and we assume that all species are present in equal concentrations. The hybridization free energies are written as $\Delta G'_{ij}$ to indicate that we use the longest complementary subsequence of strands i and j , which, due to the random sequence design, is occasionally longer than the intended domain length. To calculate the total change in base-pairing during an annealing protocol (Fig. S4b), we took the temperature derivative of the ensemble average of correctly formed base pairs,

$$\text{Hybridization} = -\frac{d}{dT} \sum_{\substack{i < j \\ j \in \mathcal{E}(i)}} l_{ij} p_{ij}(T), \quad (11)$$

where l_{ij} is the length of each hybridizing domain.

3 CLUSTER POPULATION RATIOS

We assume that annealing is slow, so that nucleation is always rate-limiting. We can write the nucleation barrier height as

$$F^\ddagger = -n^\ddagger k_B T \ln \rho_m + \varepsilon(T) E^\ddagger + C, \quad (12)$$

where n^\ddagger is the number of independent subunits in the critical nucleus, E^\ddagger is the number of 8-bp bonds in the critical nucleus, and C is a constant that accounts for the (effective) number of parallel nucleation pathways, as well as the rotational entropy terms. The bond energy ε is a decreasing function of temperature, while the per-species monomer concentration ρ_m , indicating the number of monomers per unit volume, also decreases as the reaction progresses. Initially, we have ρ_T of each species. For simplicity, let us assume that, given this initial monomer concentration, the barrier is infinitely high above some critical temperature T_0 . Nucleation begins once $T \leq T_0$, where F^\ddagger is finite. (In reality, nucleation can begin as soon as the target structure, or any large cluster, becomes thermodynamically stable. However, the

nucleation rate is proportional to $\exp(-F^\ddagger/k_B T)$, so the highest barrier that can be crossed depends on the cooling rate.)

Nucleation will proceed at a given temperature until ρ_m decreases to a point where F^\ddagger is again insurmountable. Denoting this critical barrier height by F_0^\ddagger , we can relate the final monomer concentration ρ_m at any temperature to the initial concentration at the critical temperature,

$$F_0^\ddagger - C = -n^\ddagger k_B T \ln \rho_m(T) + \varepsilon(T)E^\ddagger \quad (13)$$

$$= -n^\ddagger k_B T_0 \ln \rho_T + \varepsilon(T_0)E^\ddagger, \quad (14)$$

so that

$$\frac{\rho_T}{\rho_m} = \exp\left\{-\frac{E^\ddagger}{n^\ddagger} \left[\frac{\varepsilon(T)}{k_B T} - \frac{\varepsilon(T_0)}{k_B T_0}\right]\right\}. \quad (15)$$

Assuming that the intensity of each peak is proportional to the concentration of unassembled strands (m) or assembled structures (c), respectively, the ratio of the scattering intensities is

$$\frac{I_c}{I_m} = \frac{R_{h,c}^6}{N R_{h,m}^6} \left(\frac{\rho_T - \rho_m}{\rho_m}\right) \quad (16)$$

$$= \frac{R_{h,c}^6}{N R_{h,m}^6} \left(\exp\left\{-\frac{E^\ddagger}{n^\ddagger} \left[\frac{\varepsilon(T)}{k_B T} - \frac{\varepsilon(T_0)}{k_B T_0}\right]\right\} - 1\right), \quad (17)$$

where N is the number of distinct subunits in the target structure. Furthermore, because $\varepsilon/k_B T$ is a nearly linear function of T in the range of interest (Fig. S9), we expect the intensity ratio to have a functional form

$$\frac{I_c}{I_m} = \text{const} \times \{\exp[-a(T - T_0)] - 1\}, \quad (18)$$

where $a = (E^\ddagger/n^\ddagger)(d\beta\varepsilon/dT)$ and $\beta = 1/k_B T$. Using a linear fit to the energies as a function of temperature at temperatures of interest (Fig. S9), $d\beta\varepsilon/dT \approx 0.34 \text{ K}^{-1}$. From the theoretical free-energy profiles shown in the main text, we know that for edge BBs, $E^\ddagger/n^\ddagger = 7/6$, whilst for face BBs, the ratio is $6/5$. Hence we can estimate that $1/a \approx 2.5 \text{ K}$.

To calculate the intensity associated with each peak in the DLS data, we first fitted a sum of Gaussians to the distribution function, $f(R_h)$. We then numerically integrated the peak associated with the Gaussian function f_g , according to

$$I_{c/m} = \int_0^\infty \min[f_{g,c/m}(R_h), f(R_h)] d \ln R_h. \quad (19)$$

In reality, the appearance of aggregates at low temperatures, which tend to increase the mean R_h of the assembled population, means that the ratio of the scattering intensities is not exactly proportional to the ratio of the cluster concentrations. However, this effect is relatively small over the range of temperatures of interest (approximately 8 kelvin below T_0 ; see Fig. 4a). Instead, the exponential increase in the intensity ratio as a function of decreasing temperature shown in Fig. 5c is driven primarily by an exponential decrease in the scattering intensity of the unassembled population upon cooling below T_0 . Such behavior is consistent with the theoretically predicted evolution of the unassembled-strand population shown in Fig. 5b.

4 SUPPLEMENTAL FIGURES

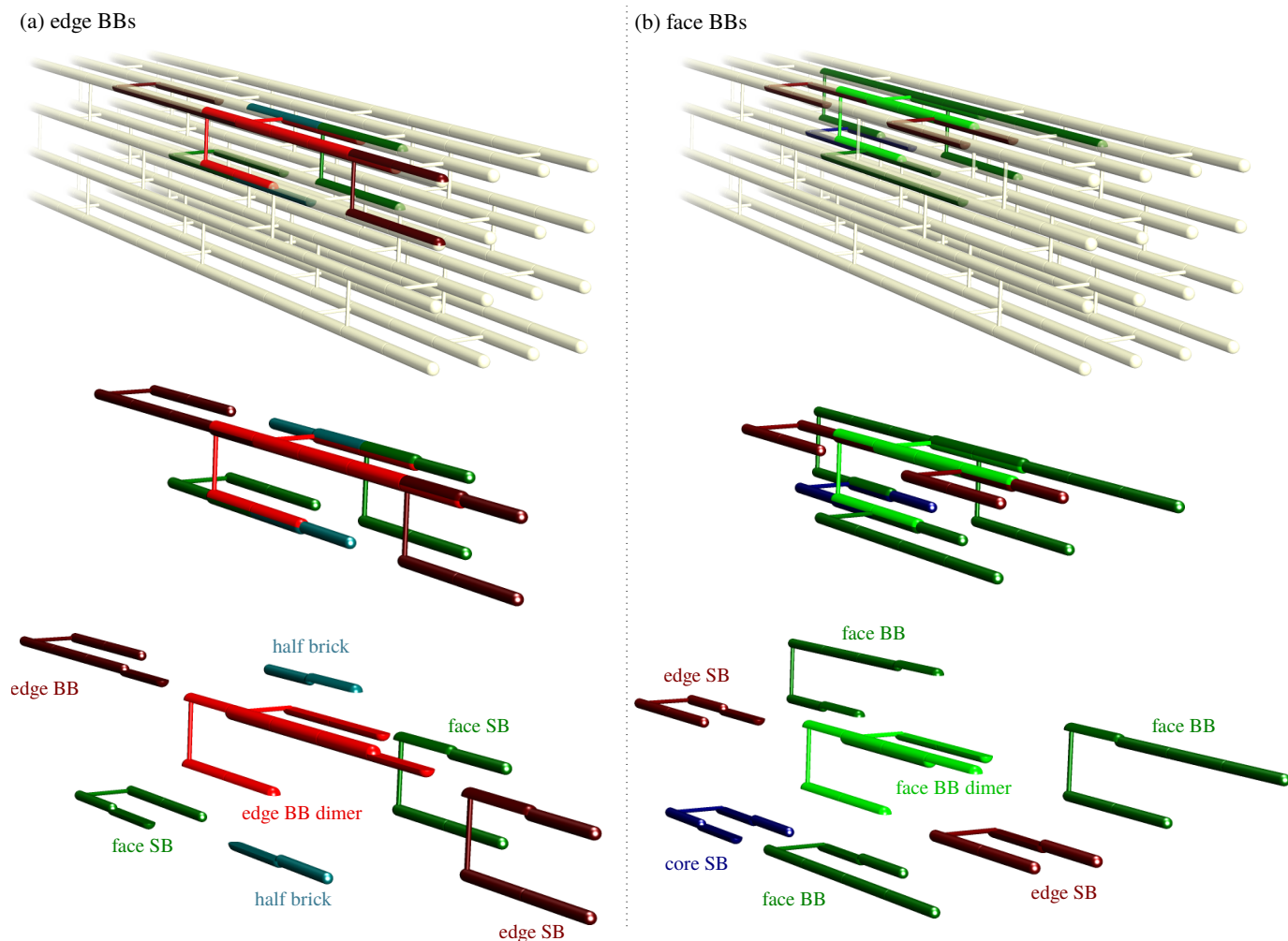


FIG. S1. Boundary brick dimers and their nearest neighbors in a schematic representation. In the top panel, the location within the target structure is shown. In the bottom panel, the neighbors are shown spread out and labeled to make their identification clearer. ‘SB’ stands for a 32-nt ‘scaffold brick’. The edge-BB system’s nucleation properties were also investigated by merging some bricks, as described in the main text. In particular, the ‘merged-A’ building block corresponds to the edge BB dimer shown in red. The ‘merged-B’ building block corresponds to the edge BB dimer and one of the face SBs shown in dark green. Either one of these face SBs could have been chosen, as both of them have direct connections to core strands. In our simulations, the face SB that is merged with the edge BB dimer is the one whose center of mass is nearer the cuboid’s principal axis in the target structure.

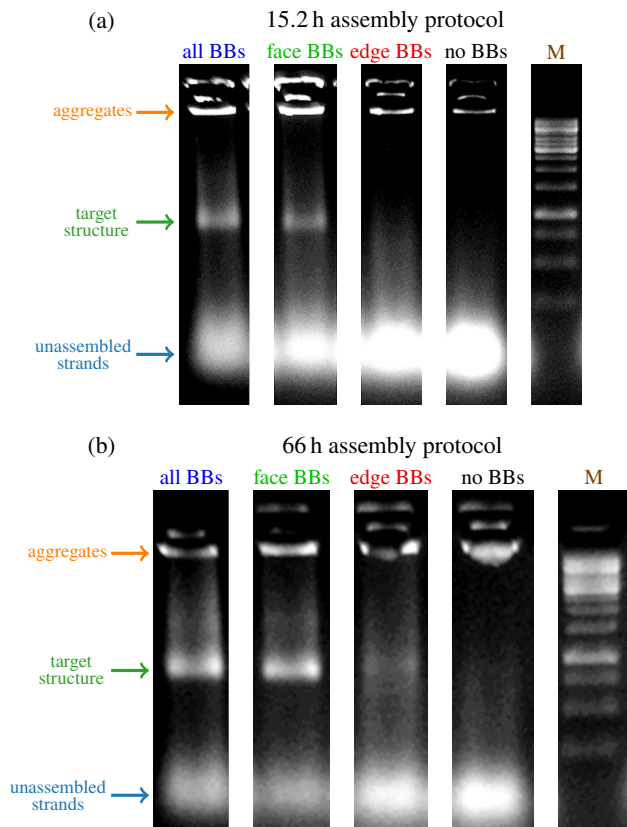


FIG. S2. Gel electrophoresis of samples at the end of (a) 15.2 hour or (b) 66 hour linear assembly protocols. Samples were assayed in 2% agarose gel. Lane M contains a GeneRuler 1 kb ladder that was used to reference the assembly yield. The bands corresponding to the target structures, unassembled strands and aggregates are indicated.

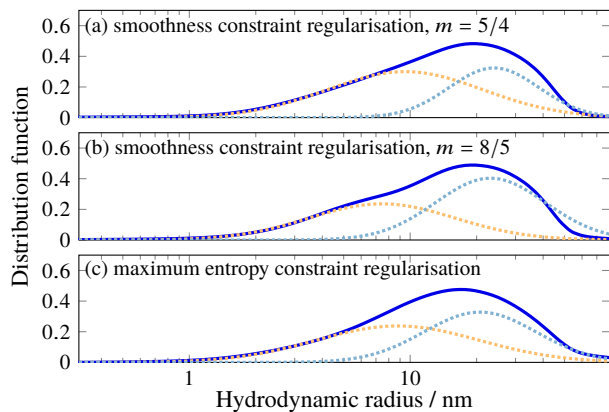


FIG. S3. Example size distribution functions (solid blue lines) for the all-BB system at 310 K determined using three regularization methods. We used a smoothness constraint functional [49] with smoothing exponents [39] of (a) $m = 5/4$ and (b) $m = 8/5$, as well as (c) a maximum entropy constraint with a Gaussian prior distribution [39]. Dotted lines show the Gaussian functions determined by fitting a linear combination of Gaussians to each distribution function.

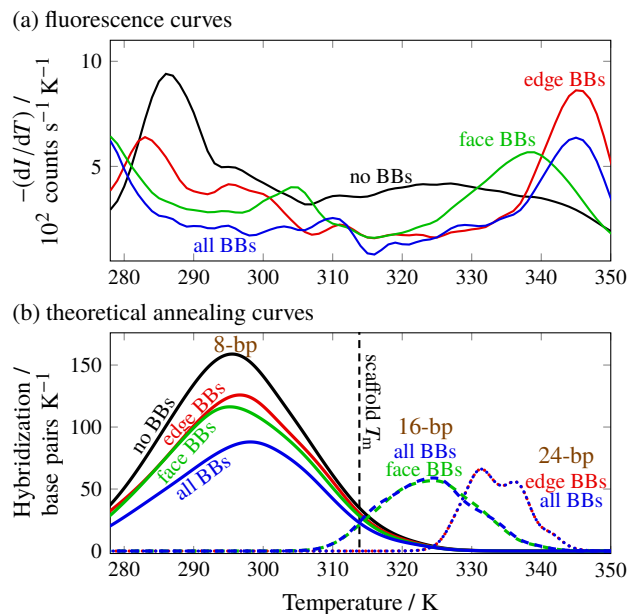


FIG. S4. (a) The derivative of the fluorescence signal I with respect to the temperature obtained from a 15.2 h annealing protocol. (b) The corresponding theoretical annealing curves (see Sec. SI-2.2). In agreement with the experimental fluorescence data, contributions from 16- (dashed lines) and 24-bp (dotted lines) hybridizations dominate at higher temperatures. The predicted scaffold-strand T_m is also shown.

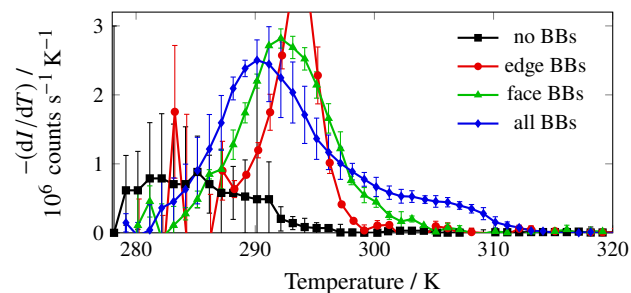


FIG. S5. The derivative of the static light scattering intensity I with respect to temperature for self-assembly following the 15.2 h annealing protocol.

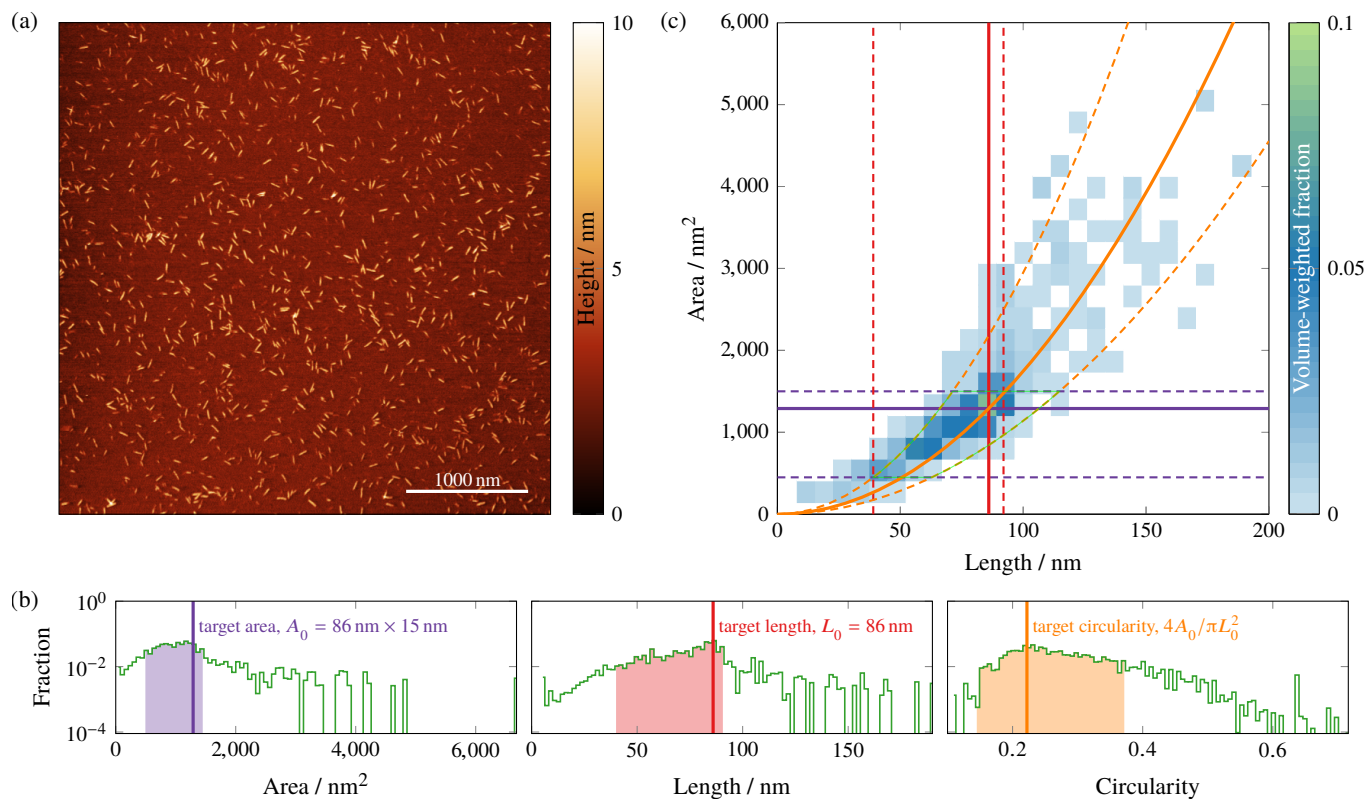


FIG. S6. Criteria for identifying target structures via AFM. (a) AFM image of the positive-control all-BB structures (see Sec. SI-1.1). (b) Area, length and circularity distributions of the particles identified in this image (see Methods). All distributions are weighted by the particle volume to prevent tiny particles from skewing the distributions. The solid vertical lines show the expected values for an ideal target structure when treating the cuboid as a cylinder with diameter $d \sim 15$ nm. (c) Two-dimensional volume-weighted distribution of imaged particle areas and lengths. The solid lines indicate the expected values for an ideal target structure, while the dashed lines correspond to the boundaries of the shaded regions in panel (b); the parabolic curves show the circularity, $4A/\pi L^2$. Notably, the peak of this distribution (green square) coincides with the expected area, length and circularity. Based on this distribution, we chose to use the area and circularity criteria ($450 \text{ nm}^2 \leq A \leq 1500 \text{ nm}^2$ and $0.145 \leq 4A/\pi L^2 \leq 0.375$, indicated by the translucent green lines) to identify particles as correctly assembled structures. Using these criteria, the AFM-determined yield of the positive control is 53%.

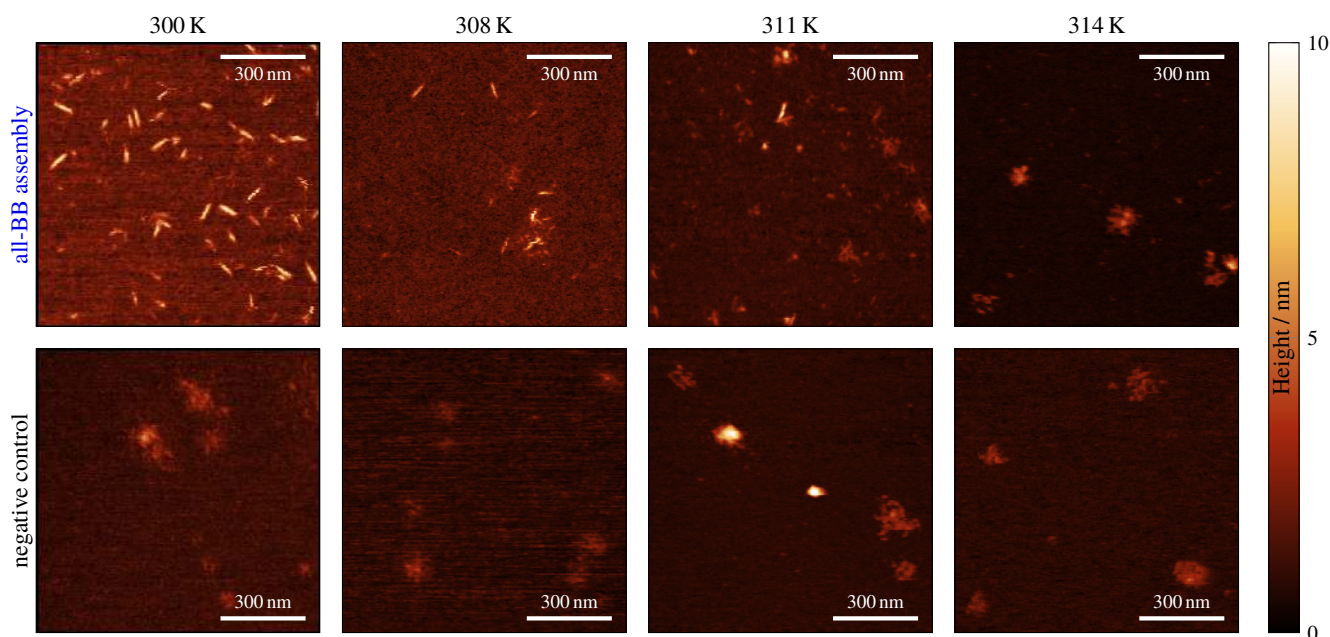


FIG. S7. AFM images for all-BB structures (top row) and negative controls (bottom row). Samples were prepared by rapidly quenching the system from the indicated temperature (column labels) during the annealing protocol (see Sec. SI-1.2). The negative control consists of a collection of similar-length oligonucleotides that were not designed to have complementary sequences. The bright amorphous clusters seen in the negative control and the all-BB structures quenched from high temperatures indicate large aggregates of oligonucleotides that form during quenching.

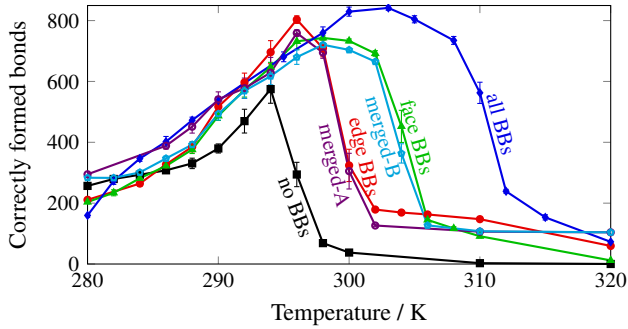


FIG. S8. The number of correctly formed bonds in the system as a function of temperature from Monte Carlo simulations. Each data point corresponds to an average over ten independent simulations in the long time limit once nucleation has occurred. Error bars give the standard deviation in each case.

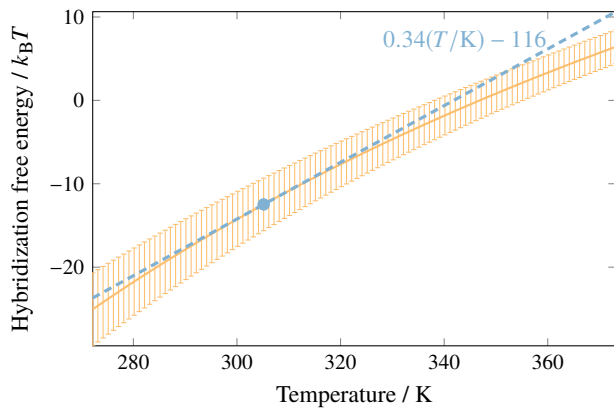


FIG. S9. The mean hybridization free energies of 8-bp interactions as a function of temperature for the no-BB structure, computed via the SantaLucia thermodynamic model [45], with error bars reflecting the standard deviation. The tangent to the curve at 305 K is also shown, demonstrating that the hybridization free energy is well described by a linear function over the region of interest (295 K to 315 K).

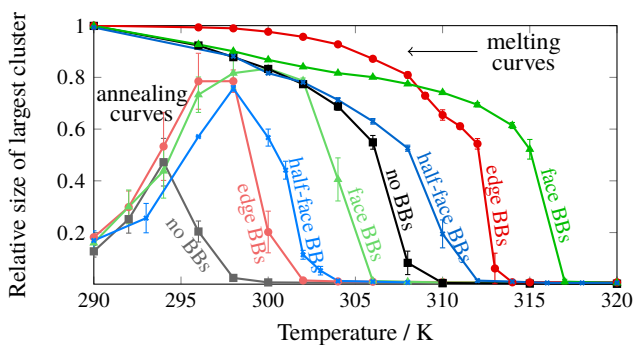


FIG. S10. Melting and annealing curves for the half-face BB structure in Monte Carlo simulations (cf. Fig. 4c and Fig. 6b).

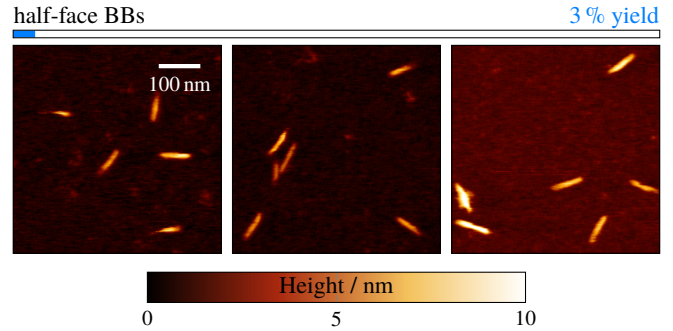


FIG. S11. AFM images and the yield, as determined by gel electrophoresis, for the half-face BB structure.

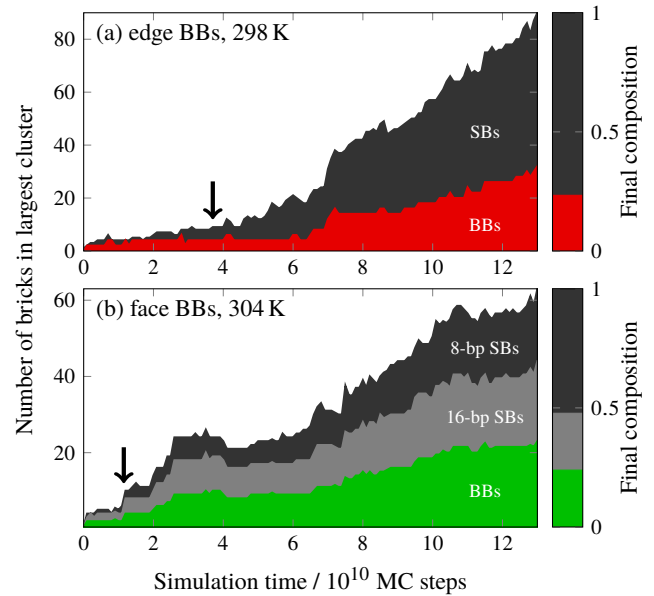


FIG. S12. The size of the largest cluster as a function of time in representative Monte Carlo trajectories for the (a) edge-BB and (b) face-BB systems. The composition of the largest cluster is shown in terms of boundary bricks (BBs) and scaffold bricks (SBs). In the face-BB system, the scaffold bricks are further divided into those that have only 8-bp hybridizations with neighboring bricks and those which form 16-bp hybridizations with face BBs. The relative proportions of each type of brick in the target structure are shown in the right-hand panel in each case. Both trajectories start at roughly the point where a fluctuation leads to nucleation and subsequent growth. Arrows indicate approximately where the theoretically predicted post-critical nucleus (see Fig. 7) first appears in each trajectory. In (a), this cluster has two BB dimers (four BBs) and four SBs. In (b), this cluster has three BB-SB dimers (three BBs and three 16-bp SBs) and two 8-bp SBs. In both cases, the cluster size increases rapidly after this nucleation event. BBs dominate in the early part of the growth phase shown here, where they comprise a greater proportion of the post-critical clusters than they do in the final assembled structure.

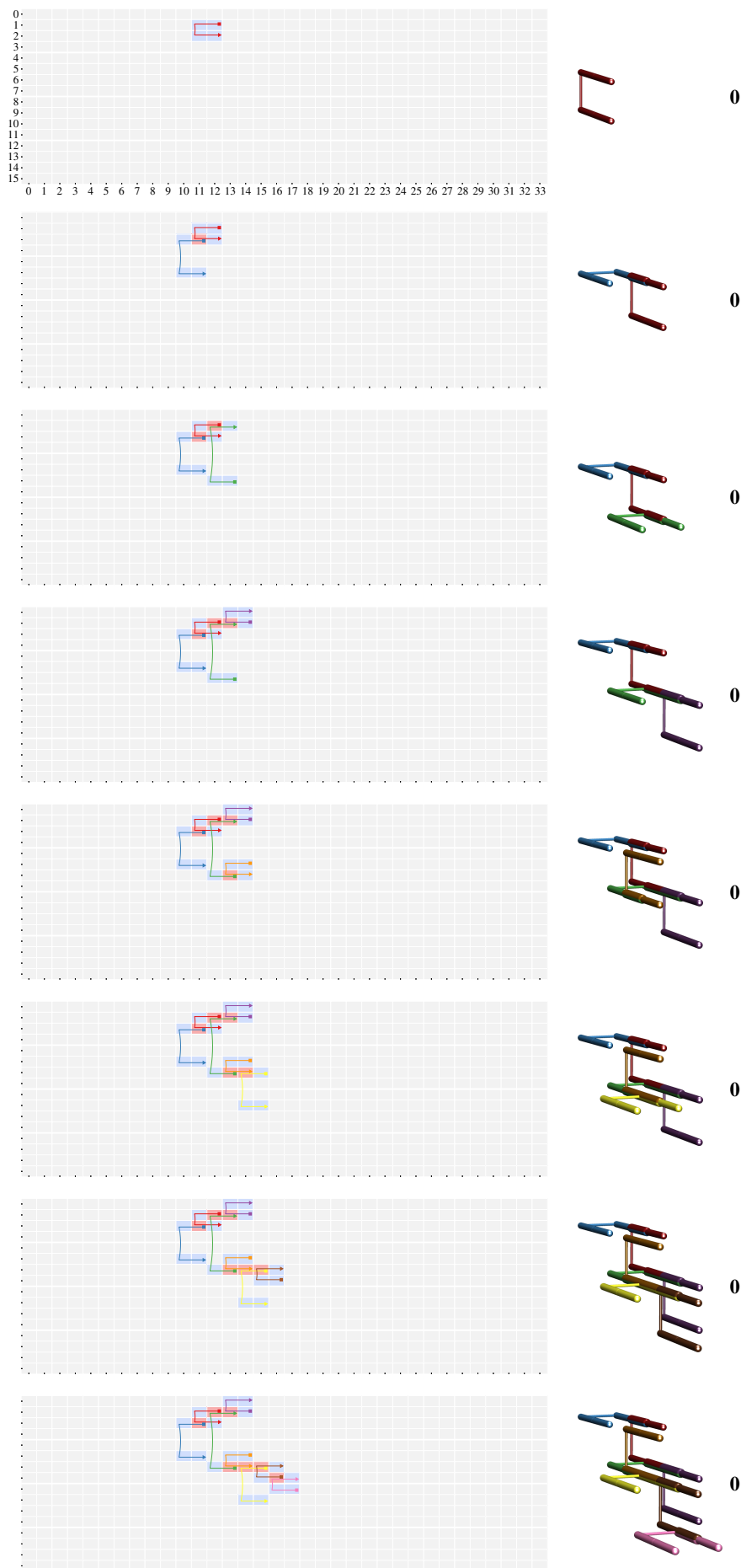


FIG. S13. Example low free-energy nucleation pathway for the no-BB system in two representations: a Cadnano-style connectivity diagram and a three-dimensional rendering. In the latter, DNA brick domains are represented by cylinders. Non-bonded domains are represented by smaller cylinders, while where two DNA bricks are bonded, larger multicolored cylinders are used. Each new monomer or multimer added to the cluster along the nucleation pathway is colored in a different hue. The bold number to the right of each structure indicates the number of multimers in the structure.

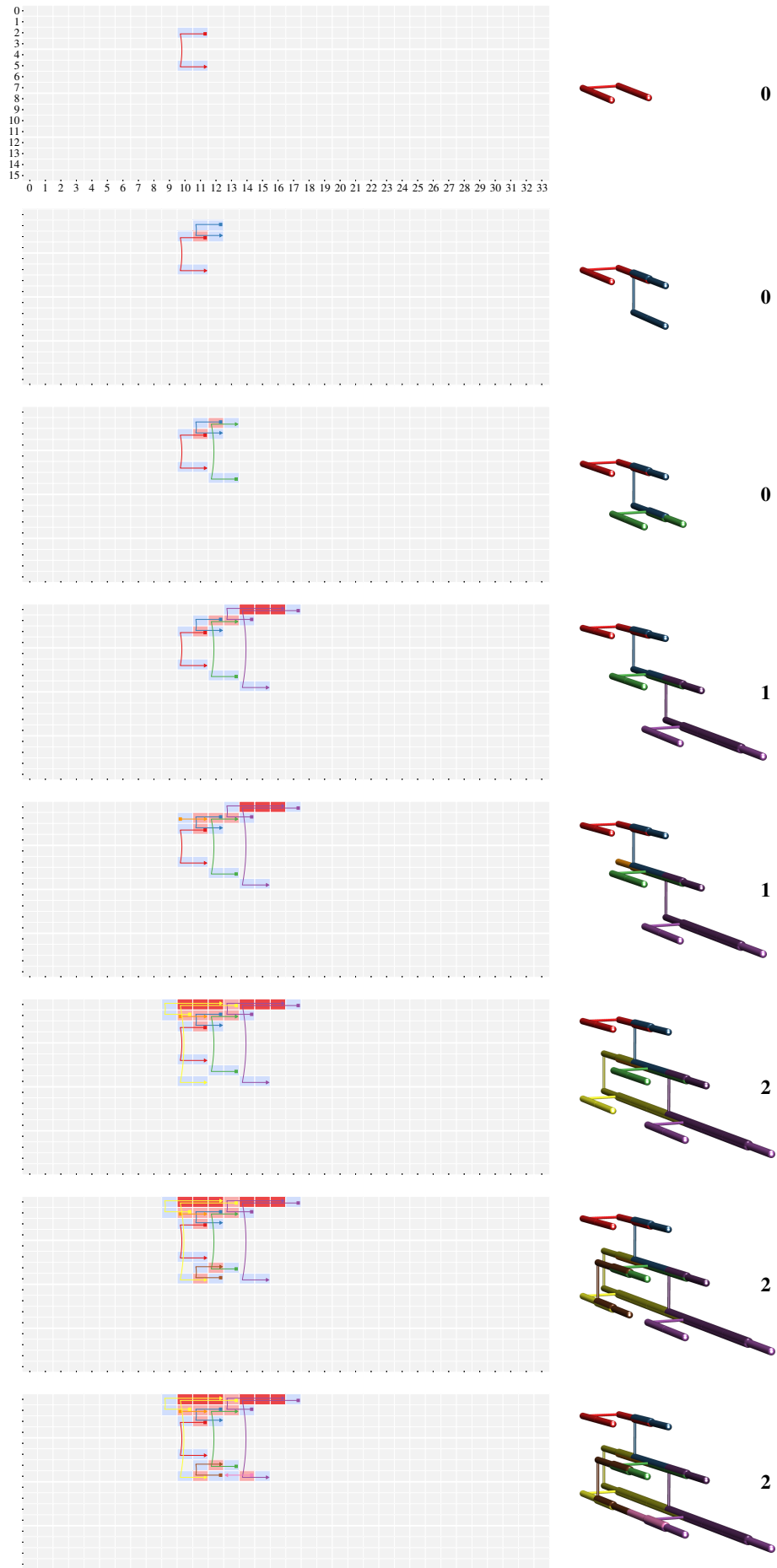


FIG. S14. Example low free-energy nucleation pathway for the edge-BB system in two representations, as in Fig. S13.

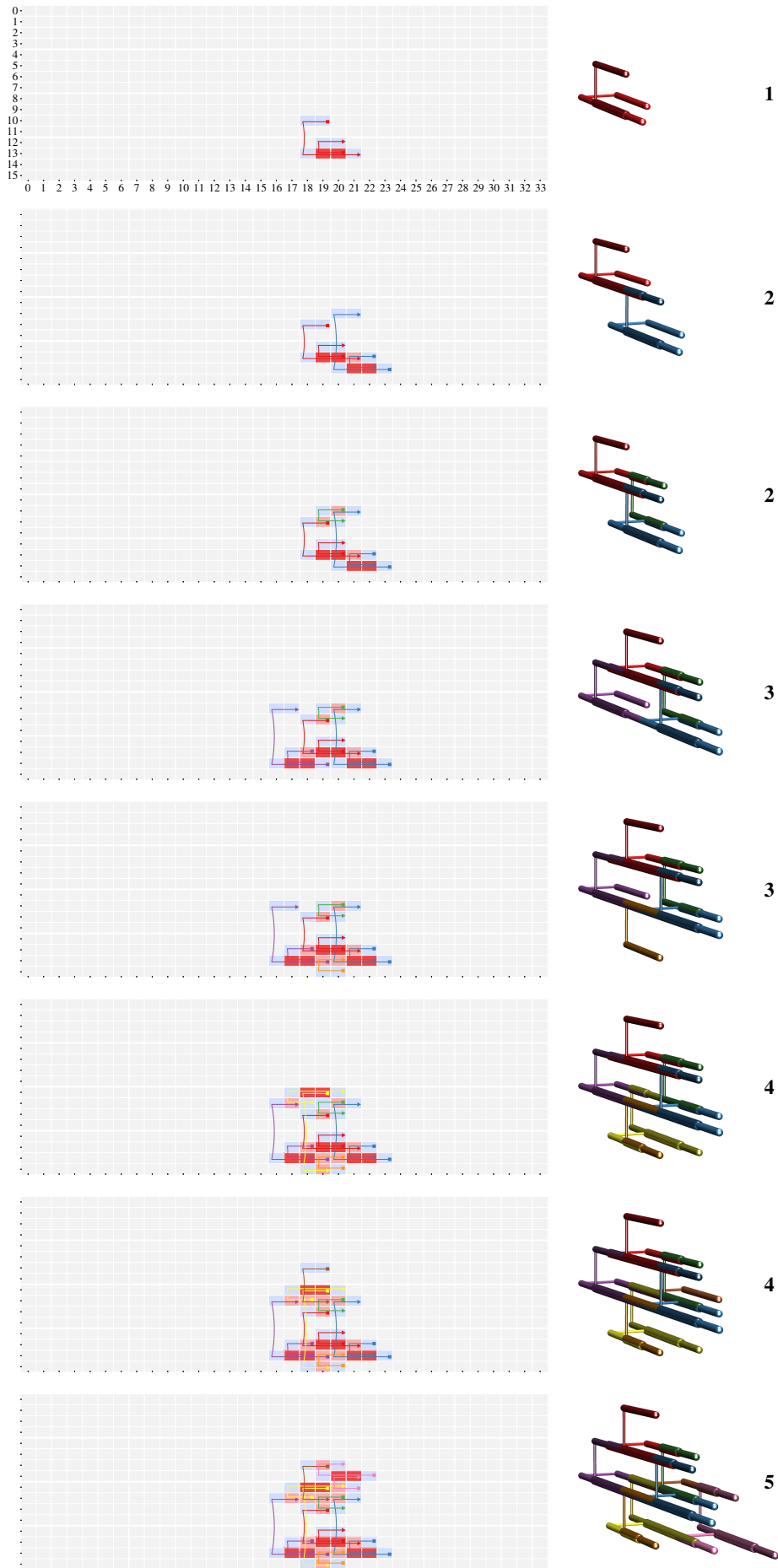


FIG. S15. Example low free-energy nucleation pathway for the face-BB system in two representations, as in Fig. S13.

5 DNA BRICK SEQUENCES

The following sequences comprise our library of DNA bricks.

ID	Sequence
1	TTCTTAAA TTTTTTTT
2	TTGGCTGA TTTTTTTT
3	TTTTTTTT CCGCGTAA
4	TTTTTTTT CCAACAGG
5	TATGGTGA TTTTTTTT
6	ATCCGAAG TTTTTTTT
7	CGCTGATC TTTTTTTT
8	TCTGATAT TTTTTTTT
9	ATATCAGA GAGCACAG
10	TCCGGGAT GGGTGCCA
11	AGAGTCTG GAGATGAT
12	GCTTCCGC CCGTGTGG
13	TAATATAA TGTCGCGC
14	AGTTAGCA TTACGCGG
15	GGAAGGAT TCATCCCC
16	TACATCTC GCCTGTCG
17	GTGCGCTT CTGTGCTC
18	TCCCTAAA GTCGAATT
19	ACCTTTTA ATCATCTC
20	GGGAGATT TAGCGGTC
21	CAGTCTTT GAGATGTT
22	AAGGTAAT GTGAAACT
23	ACATCTCG GAAAGGTT
24	CTTACACT TTCGGGAG
25	TATCAATT GCCAGAGA
26	TGCATGGG TGGTGGAT
27	ACAATGGT ATCTTTTG
28	ACCTGGTC CGTCATAC
29	GCTCTTAA TATCTTTT
30	GTTTATG AATCCGTC
31	CACCAGAA GAGCCACT
32	CCACAAGG TCTTGATG
33	TTCTTTTT CAACCAAA
34	CCGAATTA CGGTTTAC
35	CTTGCCCTG GGCCAAATA
36	CAGTCCGA CCTAGGAG
37	CGCTAAAG ATCTCCGA
38	TTCAGCAG CCTTACTC
39	GTGCTCTT GAGCGGTT
40	AAAACCTC ACATATGA
41	GGGAGCTG GCCGGGCT
42	GTTGTTCC ATAGTGGA
43	AGGTTTAA CCCAGCGG
44	CGACTCAA CCTCACAG
45	GCCGACTC GTTCAAGC
46	ACTGAGGC GAGTTAAC
47	TCATGTGG GATCTTAA
48	GATCACAA ATATGGCA
49	GAACATAA TTGCTATA
50	ACGGACTT GAAGCGAG
51	ATATAGGT CTGACACC
52	GGTGTAGG TACGCCCA
53	GGAGGTTT CTACCGAC
54	TGTTGAGG GCAGGTTA
55	AGCTTGGG AACCGTGA
56	CGACCATT TGACACCC
57	AGCTTAGC ATAGCCAG
58	GATAATAC ACTTACTC
59	GCGGAGAG AAATGGCT
60	CGTCCAGC GCATCTGT
61	AAAAGATG TCTGTGAC
62	GTCCAAGT AAGGGCAA
63	GCGTATGC TGAATATG
64	TTTAGTTT GCGTCGAA
65	ATCGTCA ATTGACGC
66	CATACACA CATATTTG
67	CTGAGCGT ATCGGTG
68	AATAGGCT ATTCAGAA
69	TAGGGCTA AAATCTGA
70	ACCATCGC AAAACGTA
71	GCGGTGCG ACGACCCC
72	GTAATGCG AAACAGG
73	TATATCCA CGGTACAT
74	TATTAAGT TTTCCCGC
75	GATCTCGA GAGATTAC
76	TACGTGTC CTCGCGCA
77	CAAATCCC TTCCATCT
78	GTTTGAC CCTGTGAT
79	CGTTTGTG ATAGGACA
80	GCAGGGTG AAGGTGAG
81	ACTCTCGT TCACTCGT
82	CCATATGA GGTCAATG

Table continues ...

ID	Sequence
83	CCAGTAAT AGCCTGAA
84	GTAGCAT CTCAAGAC
85	CCGTGCGC CCCTGCGC
86	TCTGGCGC CGGCTTAG
87	GAAAGATC ATAACGTT
88	GTCAATTT CTTTACGT
89	GAATTATA TGGTGTGT
90	CGGCGGAA CCGTCGAT
91	GGCTTGCA CTAATACG
92	TTTGTAAA CTTACCTA
93	CGGCCCGC CAAATTTA
94	AGTCTATT CTCGGTCC
95	AAGCAAGA GAAACCTA
96	TGGGCCGC GGGTTTGT
97	CTCGAATT GTGTTTCC
98	TTACTTAT AGGCGGAA
99	CTTCTACC TCTTAATG
100	TAAGTAGT CGTGTGGC
101	CCTAACAT AAACCCAG
102	GTGTAAGA GGGACATG
103	ATTACCGT CCATCCCT
104	GCCGATGG AAAACGAC
105	TCGCAACG GAAGCGTA
106	CGTAATC CACAGGAT
107	CATGGAAG CAGAGTTC
108	AACCCGCG CTAAGTCT
109	GCCTAAAG GTCCTTCC
110	CTCAGTTT AAGATTCA
111	CGCCACTC AGATCCCA
112	TCTTCAAA AGAAACCG
113	AATGTTCT CTAAGCCG
114	GAAGAGGT TCAATTTT
115	TAGGCTCT TATTGTGC
116	ACGGAAAC TCCTACCC
117	TGGCGCGA CCTAAGGT
118	GAATATCT TGTTAGCT
119	ACTCCGGC CTCCTTGG
120	ACCCCGAC ACTCGCCT
121	GGATCTCG CATGTAGC
122	GTTACCCG TATAATTA
123	GCGCAGTT TCCTTGAT
124	TTTTTCGA GGCACATC
125	CACTTACC GTGTCCTT
126	ATATTACA AAGAACGC
127	CGATCGCT GTGCGTTG
128	CTAGGGCT TAAGACCT
129	CGTCGTCT TGGGTAAG
130	CAATTCGC CGAACCCG
131	ACGTGGTC TATGTGAT
132	GCGACACA CGGCTTGC
133	CTCCGGTG GCACGTCT
134	ATTTTGGC GGAACGGG
135	GCCAGACT TTTACGGC
136	TAGCGCCG TTTGGGGA
137	GAGCTCAC CTTGACTC
138	GCGGATGC GAGGTTAG
139	TCCAATCT TTTATACC
140	AGGGATTG AGTACCBA
141	TTCCGGCG ATAAAATC
142	TCAGGGCG AGGTCTTA
143	GTACGTTT GTGCTGTT
144	TCAGCGGC AACCCGTT
145	GCATGGCC GTAGCACC
146	ATGACTCC AGGAGAGG
147	ATAACCAT CCTGGTGA
148	CTGTCATA TGCCATCT
149	TTCATTAC GTTCTACG
150	CCTACGCC GAACGGCT
151	AGTTTCTT TTGAGACT
152	AGTTAGAT CCAATGCA
153	GCGTTAAA AACCTCGT
154	CTTCGTCA CCACGTAG
155	AAGGTGTA ATGCCGAG
156	CCGACCTT GTGCTCAC
157	TCACCTGG CGCTATAC
158	TTAAGATG TGTGGCAA
159	AAGATGTT TCTACATC
160	TTACGGCG GTGATCAG
161	AAGAGCAA ACGGTATT
162	ACATGAGG AAAAATCA
163	TTACCCCT GCAGTTTC
164	TACCCAGC GTGCGGCC
165	TATTTCTT GGAAGCCT
166	CTGTGCTT ATCTATCC
167	TCCCTGTC TGTGCGAG
168	TTCTAGCC ACTGGCAC
169	CAGCTTGA CGCAAGAC
170	ATTCAGAA TCGAGACC
171	TGGACCAC GCGCTGTG

Table continues ...

ID	Sequence
172	CCATGGGT ACTGCTGT GAGGGTAA CACGTGG ACTCCTAC TGCCCGCC
173	TTCAACAA TCAAAATG ATATTGTA GCGAGATA
174	CTACATT AGCCGAGA TTCTGAAT CCGCGGCT
175	AACACTG TATGCTCT CTATCTTC GCCCTCG CATCTTAA ATATAACT
176	CTAGTAAC CGACCGTT GACAGGGA CCACCGCA TCTTCTC GTATATCA
177	CTAGGACC CAGAAGTG GTCGCTGG GGTCTAAA TAACACTT GGTCTCGA
178	TCTGATGG AGACGTCC TCAAGTCT CTGCCAG TGATTAGC GCTTAGGG
179	CATTCTAT AGCCCGCG GTTACTAG GCGCCTTG
180	GATGATCT GTGGTGGC CACAATTT GCTGGAAG
181	GAGAAAGA TCGGTGG GAGTAGT GTGATTAG AATTCCGT AAACCGGA
182	TATCCGCC TATCTCGC TACAATAT AGTTATAT CCTCATGT AACGGTCG
183	ATTAAGCT GTGGAATG TTGTTGAA CATACTCC TCATTAGG GTCACCAG
184	TTCTTAAC GCAGGTGC ATTTATGA ATAATCCT AGGAAATA CCACTGCC
185	AGGGTTCA CAGCTCCA AAGCCTGT CGAGGCGT
186	GACTCTCT CAAGGCGC AGCTTAAT TAGTAAGG
187	TTGTTTAA GCGGGGCA GTAGGAGT CCAACGTG GTGTGCGA CGGCGAGC
188	TTTTTCTG CTTCCAGC AAATTGTG GGCAGTGG GGCTAGAA CATTCCAC
189	CTTGGGGG TGATATAC CTCACTAA ACTCCTTC
190	GTCTATC CCTTACTA CCGGTACA CACCAAGA
191	AACCTACC CCCTAAGC GCTAATCA CTGGGCAG GGTCTAG GTTGCGA
192	TTACAGCG ACGCCTCG ACAGGCTT CGTCGCC AAAATGTAG CCATGAAT
193	TGTACCCG ATTCATGG AGATCATC CATTGACG TCGTTACG TTTTTTTT
194	CCTAATGA GGAGTATG GTTAGGAA TACTGTCT CCTGAATG TTTTTTTT
195	CTCCTACG CTCAATAG TGAACCTT TACTATCG
196	AGAGTTCT ACCAGCCA AGAGATGC CGAGCCCT
197	CGTAACGA CGTCAATG TTAATAACA ACAACCGA
198	CATTGAGC AGCAGGTA CAGAAAAG GAACCGAC
199	TTTTTTTT CGATAGTA GGTAGGTT TTTTTTTT
200	TTTTTTTT AGGGCTGC CCCCCAAG TTTTTTTT
201	TTTTTTTT CGGTGGAC AGAATCTT TTTTTTTT
202	TTTTTTTT TCTTGGTG CGTAGGAG TTTTTTTT
203	TTTTTTTT TCGGTGTG CGCTGTAA TTTTTTTT
204	TTTTTTTT GTGCGTTC GATAGGAC TTTTTTTT
205	TTTTTTTT TCCGGTIT AGCGAATT TTTTTTTT GCGGATA TGGCTGGT
206	TTTTTTTT GAAGGAGT TTAGTGAG TCTGCAAC ATAGAATG CTATTGAG
207	CAGACTCT TTTTTTTT TTTTTTTT GAGCCGAT
208	CAGGGTAC TTTTTTTT TTTTTTTT GGACGAGC
209	TCTGATAT TTTTTTTT TTTTTTTT GCACTGCC
210	CGCTGATC TTTTTTTT TTTTTTTT GGGGATGA
211	CAAGGGAT ATCGGCTC CTTCCGAT TCTCTGGC
212	TACATCTC GCTCGTCC TCACCATA ATCCACCA
213	AGAGTAGG GGCAGTGC TCAGCCAA ACAGTGGG
214	GGAAGGAT TCATCCCC TTTAAGAA TGATCGCA
215	TATCATTG GCCAGAGA TGCTAACT GTATGACG
216	TGATGGG TGGTGGAT CGCGAAGC TGTGTGTA
217	AGATGTTT CCCACTGT TTATATTA CAAAAGAT
218	TAACCTGG TGCATCA ATCCCGGA CACGTAAA
219	ACCTGGTC CGTCATAC TAAAAGGG AAGAGTAA
220	CCGATCAT TCACGACA AATCTCCC GCTAGATG
221	ACAATGGT ATCTTTTG AAGCGCAC GTAAACCG
222	CCGCAACC TTTACGTG TTTAGGGA ATACAAGA
223	TACCCTAC TTACTTCT AGTGTAAG CAACCCAT
224	CCAGACCG CATCTAGC ATTACCTT CACCGCTC
225	CCGAATTA CGGTTTAC CGAGATGT TTACTTGC
226	CCACAAAG TCTTGAT AAAGACTT TCGGAGAT
227	AAAGTAAT ATGGGTTG CACTAACC TATAGCAA
228	GTGCTCTT GAGCGGTG TTAAGAGC CTCGCTTC
229	TCCCAAGT GCAAGTAA AAAAGGAA TTATGAGA
230	CGGTAAAG ATCTCGCA TTCTGGTG CCAAAACT
231	GAACATAA TTGCTATA TCGGACTT TGGGCGTA
232	ACGGACTT GAAGCGAG GAAAGTTT GCGACTCA
233	ATAATAGT TCTCATAA CAGGCAAG GGTGTGAG
234	GTATGATT AGTTTTGG CTGCTGAA TGTCCGTG
235	GGTGTAGG TACGCCCA TAAACTAC TTTTCCAC
236	CTCAGCAA TGAGTCGC TTGAGTCG GTGGATAA
237	ATATAGGT CTGACACC CAGCTCCC AGGTAAGT
238	AGCAATAT CACGGACA GGAACCAAC GGGTGTCA
239	AGGGCAAC GTGGAAA TGTGATC CCCTCCCA
240	CGTGGATC TTATCCAC GCCTCAGT CCATTTCA
241	GATAATAC ACTTACCT CCAATGTA AGGTCTAC
242	CGACCATT TGACACCC GAGTCGGC CTGACAGA
243	ACAAAGTC TGGGAGGG CCTCAACA TCTTGAAT
244	CGGTATGC TGAATGG AACCCTCC TACGTTTT
245	AGTTTCTG GTAGACCT CGTAGGCT AGAGCGGT
246	AAAAGATG TCTGTGAG CCCAAGCT TAGCATAA
247	AATAGGCT ATTCAAGA GCTGGACG TCGCGGAG
248	ACCATCGC AAAACGTA AAACCTAA TGACGTTT
249	CGCACGGC ACCGCTCT CTCTCCGC CGGCGAAA
250	CAACAGTT TTATGCTA ACTTGGAC CGGGCATC
251	ATACGTGC CTCGCGCA ACGCTCAG CCGTCTG
252	ATCACCTC AAACGTCA TAGCCCTA CGGATCAA
253	TATTAAGT TTTCCGCC TGAGCGAT CAATGACC
254	TCGTATTG GATGCCCG TGTGTATG CTCACCTT
255	TCACCCTA CAGACCGG TCAGGATC ATTTTGGA
256	ATTTCCAG TTGATCCG GCATATAC AACGTTAT
257	CCATATGA GGTCAITG TGGATATC TCCGTGCA
258	GCAGGGTG AAAGTGAG CCAGCCGC GCGCAGGG
259	TGATATGG TCCAAAAT GTGCAACG GGAAACAC
260	GAAAGATC ATAACGTT GGGATTTG TTCCGCCT

Table continues ...

ID	Sequence
261	TCGTTTAC TGCACGGA ACGAGAGT GCTGGCAT
262	CCGTGCGC CCCTGCGC GACAAACG CATATCCT
263	CTCGAATT GTGTTTCC ATGCTAGC GCCACAGC
264	TTACCTAT AGGCGGAA AAATTGAC ATTTCTAC
265	ATCGACTA ATGCCAGC ATTACTGG CATTAAGA
266	AAGTAAAC AGGATATG GCGCCAGA CCACAATG
267	TAAGTAGT CGTGTGGC TCGAAGCA CTCACCTG
268	TCACGATT GTAGAAAT TTTACAAA CACGGACA
269	CTTCTACC TCTTAATG TATAATTC ATCCTGTG
270	CCGTACGC CATTTGCG TCCGGCTT TCGGTTTT
271	TAAGAGGT CAGGTGAG CCGGCCCA ATTTGACC
272	GATTCTAA TGTCCTGC AATGAGCT TGGGATCT
273	CCGTAATC CACAGGAT TCTTCTCT ATCTTAGT
274	GCCGATGG AAAACGAC GCGGGCCG GGAAGGAC
275	TGTTTACT GGTACAAT TCTTACAC TGGTAGGA
276	GACCTCTC AGATCCCA ATGTTAGG AGCTAACCA
277	ACTTGGGG ACTAAGAT CGTTGCGA ATTTTCGC
278	GCCTAAAG GTCCTTCC ACGGTAAT CCGGGGTG
279	ACGGAAAC TCCTACCC GCGGGTGT TCGCTGAG
280	GAAATATC TGTTAGCT TTTGAAGA AGGCTCCG
281	CTAATATA GCGAAAAT CTTCCATG TAAATATA
282	AGTTCGTA CACCCCCG AAACGAGG GAGAACAT
283	TTTTCGCA GGCACATC GAGCCTAC CCGTCTAT
284	CGGAATGA CCGAGCCT TCCGCCAC CCCTGACA
285	GTTACCCG TATAAATA AGAACATT GGGTTTGC
286	ACAGGACG ATGTTCTC ACCTCTTC AGGCTCTA
287	ATTCTGCT ATAGACGG AACTCGCC GTCACTGC
288	TGGTTCGA TGTACAGG GTCCGGTG TCGCTAAA
289	CAATTCCC CGAACCCG CGAATCCG AGGACGAT
290	CCTAGGCG TAAGACCT CCGCGAGT AGACGTGC
291	AGGATAAG CGAGTGAC TGTAAATC GCTGTACT
292	GCCAGACT TTTACGGC GGTAGGTT TAAGACCT
293	CGAACGAG ATCGTCTC AGACGACG GATCTCCT
294	TCTCGCTG GCACGCTC ACGACTCG TCGAACGA
295	AGGGATTG AGTACCCA TGTGTCCG AGATGGCA
296	TCAGGGCG AGGTCTTA GCGCGCTA CGTCTATT
297	CAAAGTCA AGGAGATC GACCACGT CCTCTCCT
298	ACCCGAGC TCGTTCGA GCCAAAAT CAAGGACG
299	CTGTCATA TGCCATCT GATTGGGA GAGTCCAG
300	GCACGTGA AATAGACG CCGCGGAA CAGCTCCG
301	ATGACTCC AGGAGAGG GTGAGTCC CTACGTGG
302	AAGCATCG CGTCCTTG GCATCCGC TCGCATGG
303	TTTATTGC CTGGACTC ATGTTTAT CCTCTCCC
304	TCTCGTGC CGGAGGTC GCCGCTGA GATGTAGA
305	CTTCGTCA CCACGTAG CCGCATGC AGCACGCA
306	AGTTAGAT CCATGCGA AACAGTCC GTATAGGG
307	AACGGGAT GGGAAGGG GCGGTAGG GGCCGCAC
308	AAGAATGG TCTACATC GTAATGAA GGATAGAT
309	GTCAAATA TCGCTGCT TTTAACCG TTTAGACC
310	TCACTGGG CGCTATAC AGGAAACT CGAGGGGC
311	TTACCAGC GTGCGGCC AGGTCCGG ACACGAGT
312	CTCTGCTT ATCTATCC CCGTGAAA AGGATTTA
313	GTCCGCTG GGTCTAAA TAACACTT GGTCTCGA
314	CTATCTTC GCCCTTCG CATCTTAA ATATAACT
315	CCATGGGT ACTGCTGT GAGGGTAA CACGTTGG
316	ATTATTGA ATAATCCT AGGAAATA CCACTGCC
317	ATTAGAAA TCGAGACC TTGCTCTT GGACGTCT
318	TACAATAT AGTTATAT CCTCATGT AACGGTGG
319	GTAGGAGT CCAACGTG GTGGTCCA CCGCGACG
320	AAATTGTG GGCAGTGG GGCTAGAA CATTCCAC
321	TCTGATGG AGACGTCC TCAAGCTC CTGTTCCG
322	CTAGTAAC CGACCGTT GACAGGGA CCACCGCA
323	ACAGGCTT CGTCGCCG AAATGTAG CCATGAAT
324	ATTAAGCT GTGGAATG TTGTTGAA CATACTCC
325	GCTAATCA CTGGGCAG GGTCTTAG GTTGACGA
326	GAGAAAGA TCGGTGGC CAGTAGTT GTGATTAG
327	TGTACCCG ATTCATGG AGATCATC CATTGACG
328	CCTAATGA GGAGTATG GTTAGGAA TACCTGCT
329	TTAGTGAG TCTGCAAC ATAGAATG CTATTGAG
330	AGCGAATT CTAATCAC GCGCGATA TGGCTGGT
331	ACCTTTTA ATCATCTC
332	GGGAGATT TAGCGGTC
333	CCCTACTC CACCTTTC
334	ATCCTTCC AACATCTC
335	CTTACACT TTCGGGAG
336	CCCATGCA GAAAGATA
337	ACATCTCG GAAAGGTG
338	CCAGGTTA AGTGGCTC
339	GACCAGGT CTCCTAGG
340	ATGATCGG TCATATGT
341	TTCTTTTT CAACCAAA
342	CACCAGAA GAGCCACT
343	GTAGGGTA CCGCTGGG
344	AAAACCTC ACATATGA
345	TAATTCGG AGCCCGGC
346	TTAGCAGC CCTTACTC
347	GTAGTTTA CCCAGCGG
348	GCACTCAA CCTCACAG
349	ACTTGGGA TTAGGATC

Table continues ...

ID	Sequence
350	CTTTACGC GCTTGAAC
351	GATCACAA ATATGGCA
352	AAGTCCGT GTCGGTAG
353	TCATGTGG GATCCTAA
354	AATCATA CACGGTT
355	CCTACACC ACAGATGC
356	TTGCTGAG TTCGACGC
357	AGCCTACG ATAGCCAG
358	AGCTTGGG AACCGTGA
359	GTTGCCCT CGACCGAT
360	TTTAGTTT GCGTCGAA
361	GTATTATC GCGCAAT
362	GTCCAAGT AAGGGCAA
363	CTGAGCGT ATCGGTCC
364	TAGGGCTA AAATCTGA
365	CAGAAACT ATGTACCG
366	CATCTTTT GGGGTCGT
367	GATCTCTA GAGATTAC
368	GCGATGGT GATGGGAA
369	GATATCCA CGGTACAT
370	AACTGTTG TGTCTTAT
371	GCACGTAT GTCCTGAG
372	GAGGTGAT ACGTAAAG
373	ACTCTCGT TCAGTCGT
374	CGTTTGT C ATAGGACA
375	TAGGGTGA CGTATTAG
376	GTCAATT CTTTACGT
377	TCATATGG ACACACCA
378	TCTGGCGC CGGCTTAG
379	GGCTTGCA CTAATACG
380	TTTGTA A CTTACCTA
381	GTAACGA TAGGTTTC
382	CTCGACGG TTAATTTG
383	TGGGCCCG GGGTTTGT
384	ATAGGTAA CTGGGTTT
385	AAGCAAGA GAAACCTA
386	GTTTACTT AGGGATGG
387	ACTACTTA AGACTTAG
388	AATCGTGA CGGTTTCT
389	TCGCAACG GAAGCGTA
390	ATTACCGT CCATCCCT
391	ACCTCTTA GCACAATA
392	TCTTCAA A AGAAACCG
393	GATTACGG CGGCTTAG
394	CTCAGTTT AAGATTCA
395	GTAGGCTC TATTGTGC
396	GTGGCGGA CTAAGGT
397	CCCCAAGT GCTACATG
398	CTTTAGGC CCAAGGAG
399	GCGCAGTT TCCTTGAT
400	GATATTTT AAGGACAC
401	GCGATTTC CATGTAGC
402	TACGAACT CAACGCAC
403	TGCGAAAA GCAAGCCG
404	TCATTCCG TCCCCCAA
405	CGTCGTCT TGGGTAAG
406	CGAGTCGT GTGCGTTG
407	AGCAGAAT GGTATAAA
408	TAGCCGCC TTGGGGGA
409	GGGAATTG AGTACAAG
410	ATTTTGGC GGAACGGG
411	TCCCAATC TTTATACC
412	TTCCGGCG ATAAACT
413	CTCGTTTC GGTGCTAC
414	CACGCGAG CTATGTAG
415	ATAACCAT CCTGGTGA
416	CGCCCTGA CGTAGAAC
417	GCATGCCG GTAGCACC
418	GCTCGGGT AGTCTCAA
419	TATGACAG GTGAGCAC
420	TAACGTGC CTGATCAC
421	GCGTAAA AACCTCGT
422	AGTTTCTT TTGAGACT
423	GCAATAAA GAAACTGC
424	TTACGGCG GTGATCAG
425	TGACGAAG AATACCGT
426	TTAAGATG TGTGGCAA
427	TTACCTC CAGGTTTC
428	TATTTCTT GGAAGCCT
429	TATTTGAC GTCCTGCG
430	CCCAGTGA GCTCGACA
431	TGGACCAC GCGCTGTG
432	AAGCAGAG CATTTTGA
433	CAGCTTGA CGCAAGAC
434	GAAGATAG AGAGCATA
435	ACCCATGG CGCACCAC
436	TCAATAAT GCACCTGC
437	CTAGGACC CAGAAGTG
438	AACTACTG TATGCTCT

ID	Sequence
439	ACTCCTAC TGCCCGCC
440	TTCCTAAC GCAGGTGC
441	CCATCAGA TGGAGCTG
442	TATCCGCC TATCTCGC
443	TGTTTTAA GCGGGGCA
444	CTTTTCTG CTTCCAGC
445	TGATTAGC GCTTAGGG
446	TCTTTCTC GTATATCA
447	TTACAGCG ACGCCTCG
448	TCATTAGG GTCCACCG
449	AACCTACC CCCTAAGC
450	AATTCGCT AAACCGGA
451	TCGTTACG TTTTTTTT
452	CCTGAATG TTTTTTTT
453	TTTTTTTT GAAGGAGT
454	TTTTTTTT TCCGGTTT

The following bricks were used in all structures investigated:

1, 2, 3, 4, 5, 6, 9, 10, 11, 12, 13, 14, 17, 18, 21, 22, 29, 30, 35, 36, 41, 42, 45, 46, 53, 54, 59, 60, 65, 66, 71, 72, 77, 78, 83, 84, 89, 90, 93, 94, 101, 102, 107, 108, 113, 114, 119, 120, 125, 126, 131, 132, 137, 138, 143, 144, 149, 150, 155, 156, 161, 162, 167, 168, 173, 174, 179, 180, 185, 186, 189, 190, 195, 196, 197, 198, 199, 200, 201, 202, 203, 204

In addition to the bricks common to all structures, the following bricks were used for each class of structure studied.

The **no-BB** system (330 bricks in total):

207, 208, 209, 210, 211, 212, 213, 214, 215, 216, 217, 218, 219, 220, 221, 222, 223, 224, 225, 226, 227, 228, 229, 230, 231, 232, 233, 234, 235, 236, 237, 238, 239, 240, 241, 242, 243, 244, 245, 246, 247, 248, 249, 250, 251, 252, 253, 254, 255, 256, 257, 258, 259, 260, 261, 262, 263, 264, 265, 266, 267, 268, 269, 270, 271, 272, 273, 274, 275, 276, 277, 278, 279, 280, 281, 282, 283, 284, 285, 286, 287, 288, 289, 290, 291, 292, 293, 294, 295, 296, 297, 298, 299, 300, 301, 302, 303, 304, 305, 306, 307, 308, 309, 310, 311, 312, 313, 314, 315, 316, 317, 318, 319, 320, 321, 322, 323, 324, 325, 326, 327, 328, 329, 330, 331, 332, 333, 334, 335, 336, 337, 338, 339, 340, 341, 342, 343, 344, 345, 346, 347, 348, 349, 350, 351, 352, 353, 354, 355, 356, 357, 358, 359, 360, 361, 362, 363, 364, 365, 366, 367, 368, 369, 370, 371, 372, 373, 374, 375, 376, 377, 378, 379, 380, 381, 382, 383, 384, 385, 386, 387, 388, 389, 390, 391, 392, 393, 394, 395, 396, 397, 398, 399, 400, 401, 402, 403, 404, 405, 406, 407, 408, 409, 410, 411, 412, 413, 414, 415, 416, 417, 418, 419, 420, 421, 422, 423, 424, 425, 426, 427, 428, 429, 430, 431, 432, 433, 434, 435, 436, 437, 438, 439, 440, 441, 442, 443, 444, 445, 446, 447, 448, 449, 450, 451, 452, 453, 454

The **edge-BB** system (268 bricks in total):

8, 15, 19, 23, 26, 28, 31, 34, 37, 40, 43, 47, 50, 52, 55, 58, 61, 64, 67, 70, 73, 76, 79, 82, 85, 88, 91, 95, 98, 100, 103, 106, 109, 112, 115, 118, 121, 124, 127, 130, 133, 136, 139, 142, 145, 148, 151, 154, 157, 160, 163, 166, 169, 172, 175, 178, 181, 184, 187, 191, 194, 205, 208, 210, 211, 212, 215, 217, 221, 222, 224, 226, 227, 228, 231, 233, 237, 238, 240, 242, 243, 244, 247, 249, 253, 254, 256, 258, 259, 260, 263, 265, 269, 270, 272, 274, 275, 276, 279, 281, 285, 286, 288, 290, 291, 292, 295, 297, 301, 302, 304, 306, 307, 308, 311, 313, 317, 318, 320, 322, 323, 324, 327, 329, 332, 334, 335, 336, 339, 341, 345, 346, 348, 350, 351, 352, 355, 357, 361, 362, 364, 366, 367, 368, 371, 373, 377, 378, 380, 382, 383, 384, 387, 389, 393, 394, 396, 398, 399, 400, 403, 405, 409, 410, 412, 414, 415, 416, 419, 421, 425, 426, 428, 430, 431, 432, 435, 437, 441, 442, 444, 446, 447, 448, 451, 453

The **face-BB** system (268 bricks in total):

7, 16, 20, 24, 25, 27, 32, 33, 38, 39, 44, 48, 49, 51, 56, 57, 62, 63, 68, 69, 74, 75, 80, 81, 86, 87, 92, 96, 97, 99, 104, 105, 110, 111, 116, 117, 122, 123, 128, 129, 134, 135, 140, 141, 146, 147, 152, 153, 158, 159, 164, 165, 170, 171, 176, 177, 182, 183, 188, 192, 193, 206, 207, 209, 213, 214, 216, 218, 219, 220, 223, 225, 229, 230, 232, 234, 235, 236, 239, 241, 245, 246, 248, 250, 251, 252, 255, 257, 261, 262, 264, 266, 267, 268, 271, 273, 277, 278, 280, 282, 283, 284, 287, 289, 293, 294, 296, 298, 299, 300, 303, 305, 309, 310, 312, 314, 315, 316, 319, 321, 325, 326, 328, 330, 331, 333, 337, 338, 340, 342, 343, 344, 347, 349, 353, 354, 356, 358, 359, 360, 363, 365, 369, 370, 372, 374, 375, 376, 379, 381, 385, 386, 388, 390, 391, 392, 395, 397, 401, 402, 404, 406, 407, 408, 411, 413, 417, 418, 420, 422, 423, 424, 427, 429, 433, 434, 436, 438, 439, 440, 443, 445, 449, 450, 452, 454

The half-face-BB system (299 bricks in total):

7, 16, 20, 32, 38, 39, 44, 56, 62, 63, 69, 80, 86, 87, 92, 104, 110, 111, 117, 128, 134, 135, 141, 152, 158, 159, 165, 176, 182, 183, 188, 207, 209, 211, 213, 214, 215, 216, 217, 218, 219, 220, 221, 223, 225, 227, 229, 230, 231, 232, 233, 234, 235, 236, 237, 239, 241, 243, 245, 246, 247, 248, 249, 250, 251, 252, 253, 255, 257, 259, 261, 262, 263, 264, 265, 266, 267, 268, 269, 271, 273, 275, 277, 278, 279, 280, 281, 282, 283, 284, 285, 287, 289, 291, 293, 294, 295, 296, 297, 298, 299, 300, 301, 303, 305, 307, 309, 310, 311, 312, 313, 314, 315, 316, 317, 319, 321, 323, 325, 326, 327, 328, 329, 330, 331, 333, 335, 337, 338, 339, 340, 341, 342, 343, 344, 345, 347, 349, 351, 353, 354, 355, 356, 357, 358, 359, 360, 361, 363, 365, 367, 369, 370, 371, 372, 373, 374, 375, 376, 377, 379, 381, 383, 385, 386, 387, 388, 389, 390, 391, 392, 393, 395, 397, 399, 401, 402, 403, 404, 405, 406, 407, 408, 409,

411, 413, 415, 417, 418, 419, 420, 421, 422, 423, 424, 425, 427, 429, 431, 433, 434, 435, 436, 437, 438, 439, 440, 441, 443, 445, 447, 449, 450, 451, 452, 453, 454

The all-BB system (206 bricks in total):

7, 8, 15, 16, 19, 20, 23, 24, 25, 26, 27, 28, 31, 32, 33, 34, 37, 38, 39, 40, 43, 44, 47, 48, 49, 50, 51, 52, 55, 56, 57, 58, 61, 62, 63, 64, 67, 68, 69, 70, 73, 74, 75, 76, 79, 80, 81, 82, 85, 86, 87, 88, 91, 92, 95, 96, 97, 98, 99, 100, 103, 104, 105, 106, 109, 110, 111, 112, 115, 116, 117, 118, 121, 122, 123, 124, 127, 128, 129, 130, 133, 134, 135, 136, 139, 140, 141, 142, 145, 146, 147, 148, 151, 152, 153, 154, 157, 158, 159, 160, 163, 164, 165, 166, 169, 170, 171, 172, 175, 176, 177, 178, 181, 182, 183, 184, 187, 188, 191, 192, 193, 194, 205, 206